Mode-{I, III} multiaxial fatigue of welded joints in steel maritime structures
Total stress based resistance incorporating strength and mechanism contributions

Bufalari, Gabriele; den Besten, Henk; Hong, Jeong Kyun; Kaminski, Miroslaw Lech

DOI
10.1016/j.ijfatigue.2024.108499

Publication date
2024

Document Version
Final published version

Published in
International Journal of Fatigue

Citation (APA)
Bufalari, G., den Besten, H., Hong, J. K., & Kaminski, M. L. (2024). Mode-{I, III} multiaxial fatigue of welded joints in steel maritime structures: Total stress based resistance incorporating strength and mechanism contributions. *International Journal of Fatigue*, *188*, Article 108499. https://doi.org/10.1016/j.ijfatigue.2024.108499

International Journal of Fatigue 188 (2024) 108499

Contents lists available at ScienceDirect

International Journal of Fatigue

journal homepage: www.elsevier.com/locate/ijfatigue

Mode-{I, III} multiaxial fatigue of welded joints in steel maritime structures: Total stress based resistance incorporating strength and mechanism contributions

Gabriele Bufalari [a], Henk den Besten [a,*], Jeong Kyun Hong [b], Miroslaw Lech Kaminski [a]

[a] Maritime and Transport Technology Department, Delft University of Technology, Delft, The Netherlands
[b] Thornton Tomasetti, 120 Broadway, New York, NY 10271, United State of America

ARTICLE INFO

Keywords:
Fatigue
Multiaxiality
Welded joints
Strength and mechanism
Total stress

ABSTRACT

Arc-welded joints in steel maritime structures are typically identified as weakest links in terms of fatigue limit state performance. Multiaxiality can be involved, consisting of predominant mode-I and non-negligible mode-III components. Aiming to answer the question if a cracked geometry based fatigue strength parameter would outperform an intact geometry based one like the effective notch stress, the total stress is adopted. A von Mises type of criterion is defined at the critical fracture plane and includes mode specific and material characteristic strength and mechanism contributions. A lifetime dependent shear strength coefficient is introduced to cover the resistance curves intercepts and slopes, whereas the total stress parameter contains the mean stress contribution as well as the (mixed) mode dependent notch and crack tip elastoplasticity coefficients, reflecting an interaction mechanism. Cycle counting includes a cycle-by-cycle non-proportionality measure and damage accumulation is based on a linear model. Evaluating mid-cycle fatigue resistance data, the total stress and effective notch stress performance turns out to be similar. However, the total stress related elastoplasticity coefficients are an explicit and sensitive measure to incorporate the actual physics of the fatigue damage process, whereas the material characteristic lengths for the effective notch stress seem to be more implicit and less sensitive ones.

1. Introduction

Maritime structures, as well as civil and aerospace ones – like ships, trains and airplanes, respectively – experience cyclic loading induced response conditions. Fatigue: a local, progressive, crack development damage process [1], is typically a governing limit state [2–5]. For commonly applied metals like steel and aluminium, arc-welded joints often connecting the planar or tubular structural members are identified as weakest links in that respect. The notched geometries involved are introducing hot spots, explaining the fatigue sensitivity [6].

If the structural response conditions are multiaxial, either proportional (P) or non-proportional (NP), loading and geometry sources generally provide the contributions. Environment and service induced external loading components, like wind and waves from different directions, may occur simultaneously. Changing geometry induced stiffness variations enable multiple – internal – load transfer mechanisms along dissimilar paths.

Since the (curved) plate thickness is often relatively small in comparison to the other structural member dimensions and the external loading is typically a distributed one, the internal mode-I loading components: normal force F_n as well as the in-plane and out-of-plane bending moments M_b, are typically governing (Fig. 1). At the same time, the shear force F_s and torsion moment M_t mode-III components affect in specific cases [7,8] the predominant mode–I response and multiaxiality has to be taken into account for accurate fatigue strength and life time estimates [e.g. 9].

The fatigue damage process involves an initiation and growth contribution [1] and can be modelled adopting respectively an intact and cracked geometry parameter to establish the fatigue strength S and obtain a life time estimate N [10]. Since far field response spectra of welded joints in steel maritime structures reflect predominantly linear elastic behaviour, S is typically of the stress – rather than strain or energy – type, in particular for mid- and high-cycle fatigue [11]. Correlation of S and N often reveals a log–log linear relation and a Basquin type of formulation is naturally adopted: $\log(N) = \log(C) - m \cdot \log(S)$. Intercept $\log(C)$ and slope m are respectively the strength and damage mechanism coefficients, suggesting the mode-I and mode-III values are different.

A major part of the fatigue life time N is predominantly spent in the notch affected region, rather than the far field dominated one [12], suggesting S could be a notch characteristic intact geometry parameter.

---

[*] Corresponding author.
E-mail address: henk.denbesten@tudelft.nl (H. den Besten).

https://doi.org/10.1016/j.ijfatigue.2024.108499
Received 11 April 2024; Received in revised form 16 June 2024; Accepted 10 July 2024

Nomenclature

Symbols

α	(half) notch angle
β_a	particular stress angle
$\beta(N)$	lifetime dependent shear strength coefficient
γ	response ratio coefficient
Δ	prefix indicating stress range
θ	generic (stress) angle
$\{\lambda_{\sigma a}, \lambda_{\sigma s}\}$	mode-I eigenvalue of (anti-)symmetry part
λ_τ	mode-III eigenvalue
$\{\mu_{\sigma a}, \mu_{\sigma s}\}$	mode-I equilibrium coeff. of (anti-)symmetry part
$\mu_{\tau F}$	mode-III force equilibrium coefficient
$\mu_{\tau M}$	mode-III moment equilibrium coefficient
ρ	(real) weld notch radius
ρ^*	material characteristic length
σ	normal stress
σ_{fe}	mode-I linear structural field stress
σ_N	fatigue lifetime standard deviation
$\sigma_n\ (r/t_p)$	weld toe notch stress distribution
σ_s	(structural) normal stress
σ_{se}	mode-I self equilibrium stress
σ_{sb}	M_b induced structural normal stress component
σ_{sm}	F_n induced structural normal stress component
τ	shear stress
τ_{fe}	mode-III linear structural field stress
$\tau_n\ (r/t_p)$	mode-III weld toe notch shear stress distribution
τ_s	(structural) shear stress
τ_{se}	mode-III self equilibrium stress
τ_{ss}	F_s induced structural shear stress component
τ_{st}	M_t induced structural shear stress component
Φ	parameter vector
$\{\chi_{\sigma a}, \chi_{\sigma s}\}$	mode-I eigenvalue coeff. of $\{\lambda_{\sigma a}, \lambda_{\sigma s}\}$
a	crack size
a_f	final crack size
a_i	initial crack size
C	fatigue resistance curve intercept
C_{bw}	weld load carrying normal stress coefficient
C_{np}	path characteristic non-proportionality coefficient
c_m	material characteristic non-proportionality coeff.
C_{tw}	weld load carrying shear stress coefficient
f_n	line normal force
F_n	nodal normal force
f_s	line shear force
F_s	nodal shear force
h_w	weld leg height
I_N	notch crack growth integral
K	stress intensity factor
l_w	weld leg length
m	fatigue resistance curve slope
m_b	line bending moment
M_b	nodal bending moment
M_{kn}	$\mathcal{S}_t$ related notch factor
m_t	line torsion moment
M_t	nodal torsion moment
n	elastoplasticity coefficient
n_i	number of counted cycles
N	fatigue lifetime in number of cycles
r_0	radial distance coordinate system origin to notch tip
r	radial coordinate
r_{σ_s}	structural normal stress ratio
r_{τ_s}	structural shear stress ratio
R	response ratio
R_r	response ratio including $\mathcal{S}_r$
R_t	tube outer radius
S	fatigue strength parameter
$\mathcal{S}_r$	(mean) residual stress
$\mathcal{S}_e$	effective notch stress parameter
$\mathcal{S}_t$	traction equivalent stress parameter
$\mathcal{S}_T$	total stress parameter
t_b	base plate thickness
t_c	cross plate thickness
t_p	plate thickness
$T_{\sigma S}$	10%–90% strength scatter band index
Y_f	far field factor
Y_{fb}	far field factor bending component
Y_{fm}	far field factor membrane component
Y_{fs}	far field factor shear component
Y_{ft}	far field factor torsion component
Y_n	notch factor
$\mathcal{L}$	log-likelihood
I	mode-I index
III	mode-III index

Abbreviations

AW	as-welded
CA	constant amplitude
DS	double side
FE	finite element
NP	non-proportional
P	proportional
SIF	stress intensity factor
SR	stress-relieved
VA	variable amplitude

Different fatigue strength parameters have been developed over time aiming to obtain more accurate life time estimates, balanced with parameter complexity and computational efforts [13]. Incorporating local (notch) information provides more generalised S formulations and the number of involved fatigue resistance curves reduces accordingly (i.e. ultimately to one), like for the effective notch stress concept [13–19]. Taking advantage of the semi-analytical weld notch stress distribution expressions [13,20], the effective notch stress $\mathcal{S}_e$ can be calculated averaging the notch stress distribution along the expected crack path over a material characteristic length ρ^*; another mechanism parameter, meaning solid finite element (FE) models to estimate $\mathcal{S}_e$ are not required anymore. Uniaxial mode-I and mode-III investigations for welded joints in steel maritime structures revealed distinguished $\{\rho^*_I, \rho^*_{III}\}$ as well as $\{\log(C_I), \log(C_{III})\}$ and $\{m_I, m_{III}\}$ values [11,13,20]. Since a response cycle needs two parameters for a complete spatial description, e.g. range and ratio, mode specific response ratio coefficients $\{\gamma_I, \gamma_{III}\}$; strength parameters, have been discovered as well [11,13,20].

For multiaxial fatigue assessment in the time domain, a mode-I equivalent von Mises type of failure criterion has been established at the critical fracture plane [21]. Rather than a constant, a life time

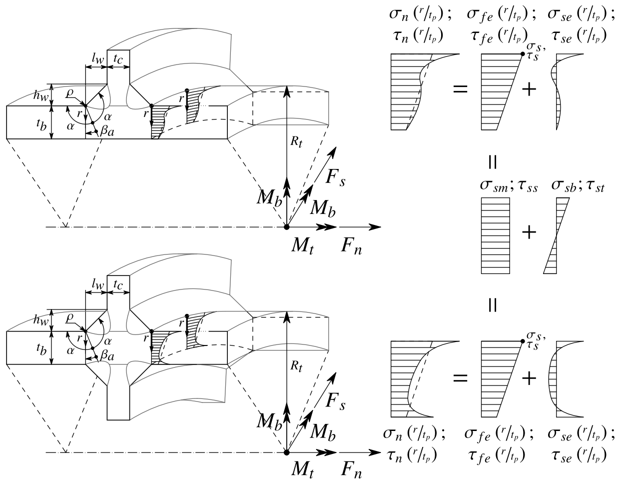

Fig. 1. Linear superposition of an equilibrium equivalent and self-equilibrium part for the mode-{I, III} weld toe notch stress distributions of a DS welded T-joint and DS welded cruciform joint in a tubular structure.

dependent shear strength coefficient $\beta(N)$ has been introduced to cover the mode specific and material characteristic $\{\log(C), m\}$, whereas S_e explicitly contains $\{\gamma, \rho^*\}$. Counting at the von Mises plane, the cycle-by-cycle non-proportionality measure includes a response path and material contribution. A 1^{st} order response approach shows the best performance. Damage accumulation is based on a linear model. However, despite the impressive outperformance in comparison to other combinations of failure criterion, damage plane, cycle counting algorithm, non-proportionality measure and damage accumulation model, the P data shows a relatively large data scatter. Multiaxial mode-{I, III} coupling seems incomplete and involving the mode specific and material characteristic parameters only is likely insufficient. Adopting a von Mises type of failure criterion – without mode-{I, III} coupling by definition – and corresponding cycle counting plane and algorithm could be an explanation, as well as the involved intact geometry parameter S_e rather than a cracked geometry one.

Since the notches inevitably contain welding induced defects, adopting a notch characteristic cracked geometry parameter like the total stress S_T [10,11,13,22] to establish the fatigue strength seems justified as well. The actual initiation (i.e. nucleation) contribution to the total fatigue life time is virtually eliminated and growth is governing.

For S still of the stress type, the intact geometry related semi-analytical weld notch stress distribution formulations can be turned into cracked geometry ones, introducing the weld notch stress intensity factor (SIF) K. Cyclic loading & response conditions turn K into a crack growth driving force ΔK and defects may develop into cracks. Since the growth rate initially shows elastoplastic wake field affected anomalies [22], a modified Paris' equation has been established, including the weld notch- and far field characteristic contributions: a generalised two-stage crack growth relation. Applying an integral operator provides a log–log linear resistance relation of the Basquin type, correlating the fatigue life time N and an equivalent fatigue strength parameter: the total stress S_T [10,22]. Uniaxial mode-I intercept $\log(C_I)$ and slope m_I, as well as response ratio coefficient γ_I and elastoplasticity coefficient n_I estimates have already been obtained for welded joints in steel maritime structures [11,13]. The S_T and S_e performance in terms of life time scatter σ_N and strength scatter band index $T_{\sigma S}$ proved to be similar.

Whereas ρ^* is a mode specific and material characteristic length defining S_e to incorporate the notch stress gradient, S_T includes the stress (intensity) gradient along the full plate thickness t_p defined final crack length a_f, suggesting ρ^* and a_f serve the same purpose. However, S_T contains an additional mechanism related parameter n and may increase insight in the mode specific and material characteristic behaviour. The uniaxial mode-III and multiaxial mode-{I, III} S_T performance have not been established before and a key question is if the mode coupling is equally important for S_T as for S_e. At the same time, a cracked geometry parameter seems one step closer to the actual damage process than an intact one, hypothesising a fatigue strength parameter S_T may outperform S_e for multiaxial fatigue.

The intact geometry related weld notch stress distribution will be translated first to a cracked geometry equivalent weld notch stress intensity distribution (Section 2), providing input for S_T. Considering all relevant assessment aspects for a time domain approach, including type of criterion, damage plane selection, cycle counting aspects including ways to deal with non-proportionality and damage accumulation [21], the S_T performance will be evaluated for multiaxial fatigue resistance data of welded joints in steel maritime structures (Section 3). Mode specific and material characteristic strength and mechanism contributions, $\{\log(C), \gamma\}$ and $\{m, n\}$ respectively, will be established. A comparison to S_e as well as another cracked geometry parameter: the traction equivalent structural stress S_t [23–27], will be provided for reference purposes.

2. Weld notch stress (intensity) distributions

Although mode-I and mode-III through-thickness weld notch stress distribution formulations along the expected (2D) crack path $\{\sigma_I(r/t_p), \tau_{III}(r/t_p)\}$ – key elements for a fatigue design criterion – are separately established before [11,13,20,22], a short recapitulation is provided (Section 2.1) in order to discuss the differences, as well as to present a comparison to bi-linear approximations [28]. At the same time, the intact geometry related $\{\sigma_I(r/t_p), \tau_{III}(r/t_p)\}$ are used to obtain the cracked geometry equivalent weld notch stress intensity distributions (Section 2.2): $\{K_I(a/t_p), K_{III}(a/t_p)\}$. Mode-I formulations for planar structures are already available [13,22], but modifications turned out to be required for tubular ones. Sufficiently accurate mode-III formulations seem to be still lacking in literature and have been derived for both planar and tubular structure configurations [20]. Last but not least, a comparison to the bi-linear approximation based $\{K_I(a/t_p), K_{III}(a/t_p)\}$ formulations [28] is provided.

2.1. Weld notch stress distributions

Adopting a linear superposition principle [22], equilibrium equivalent and self-equilibrium parts $\{\sigma_{fe}, \sigma_{se}; \tau_{fe}, \tau_{se}\}$ have been distinguished (Fig. 1) in order to formulate $\{\sigma_I(r/t_p), \tau_{III}(r/t_p)\}$. Three components are involved: the notch stress, the weld-load carrying stress and the far field stress. Typically three zones can be identified in all distributions: the zone 1 peak stress value, the zone 2 notch-affected stress gradient and the zone 3 far-field dominated stress gradient, demonstrating stress field similarity.

The V-shaped notch angle characteristic stress component applies to both groove and fillet welds and represents the (near) singular contribution defining the hot spot [13,20,22].

Since the weld geometry causes a local change in stiffness, the notch becomes load carrying up to some extent, depending on the joint dimensions including welding penetration level as well as loading conditions. Weld notch load carrying stress component estimates can be obtained using beam FE models, but polynomial fitting functions turned out to be more useful from engineering perspective [13,20].

The equilibrium equivalent far field stress components $\{\sigma_{fe}, \tau_{fe}\}$ in the cross-section at a weld toe (Fig. 1) is in compliance with the fracture mechanics definition [23,29]. Estimates are naturally obtained using through-thickness linearisation rather than surface extrapolation [30] adopting a relatively coarse meshed shell/plate FE model (Fig. 2) [31,32]. Transforming the nodal normal and shear forces $\{F_{n,i}, F_{s,i}\}$ as well as bending and torsion moments $\{M_{b,i}, M_{t,i}\}$ along the weld seam to

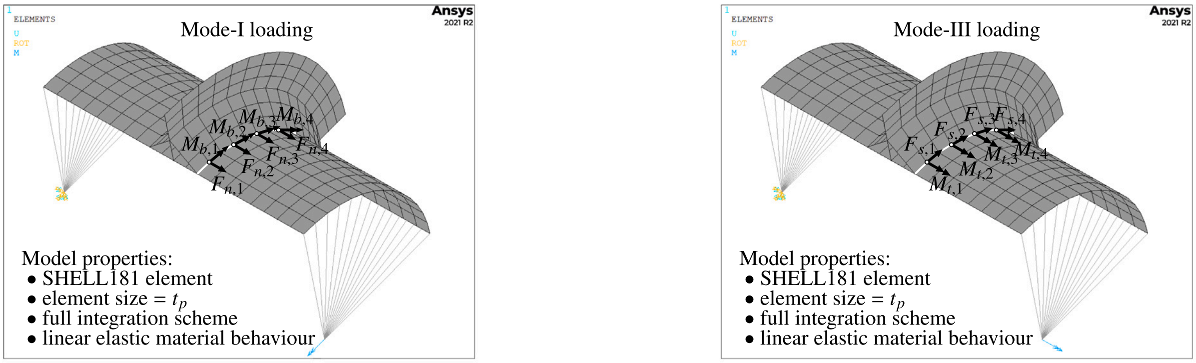

(a) (b)

Fig. 2. Part of a shell FE model of a (non-symmetric) T-joint in a tubular structure for a mode-I (a) and mode-III (b) response.

line forces and moments $\{f_{n,i}, f_{s,i}\}$ and $\{m_{b,i}, m_{t,i}\}$, four systems of equations have to be solved for: $\{F_n\} = [T]\{f_n\}$, $\{F_s\} = [T]\{f_s\}$, $\{M_b\} = [T]\{m_b\}$ and $\{M_t\} = [T]\{m_t\}$ [23,24,33]. The constant membrane and linear bending terms $\{\sigma_{sm}, \sigma_{sb}\}$, as well as the constant shear and linear torsion ones $\{\tau_{ss}, \tau_{st}\}$ for respectively mode-I and mode-III [32] can be calculated accordingly to acquire the structural stresses $\{\sigma_s = \sigma_{sm} + \sigma_{sb}, \tau_s = \tau_{ss} + \tau_{st}\}$ and structural stress ratios $\{r_{\sigma s} = \sigma_{sb}/\sigma_s, r_{\tau s} = \tau_{st}/\tau_s\}$ as characteristic far field stress parameters.

If the welded joint structural stiffness – either in planar or tubular structures – does not significantly affect the stress distribution, like in general for groove welds (e.g. in butt joints), the weld does not need to be modelled and the far field stress information can be obtained at the intersection line of the connected structural members [29]. However, fillet weld modelling is typically required (e.g. in T-joints and cruciform joints) for more accurate far field stress estimates – although avoided in some guidelines for engineering purposes [34] –, in particular if a structural response contains superimposed contributions from different levels of stiffness hierarchy, like often applies to maritime structures. Considering for example a stiffener-frame connection as a critical fatigue sensitive location in the bottom structure of a ship sailing in quartering seas, the mode-{I, III} far field stress consists at least of a local water pressure and shear force induced response at plate-stiffener level, as well as a bending moment and torsion moment induced one at global hull girder level [35,36]. Inclined shell elements have been used (Fig. 2), rather than inclined rigid ones or shell elements with increased local thickness at the joint location [32,37].

2.1.1. Mode-I formulation

For non-symmetry with respect to half the plate thickness $(t_p/2)$ and notch radius $\rho = 0$, the mode-I weld toe notch formulation yields [21]:

$$\sigma_n\left(\frac{r}{t_p}\right) = \sigma_s\left[\sigma_{se}\left(\frac{r}{t_p}\right) - 2r_{\sigma_s}\left(\frac{r}{t_p}\right)\right] \tag{1}$$

with σ_{se} being the self equilibrium stress part (Appendix A). Similar formulations are available for symmetry with respect to $(t_p/2)$ as well as for the $\rho > 0$ cases [22].

A non-monotonic and monotonically increasing weld notch stress distribution at the weld toe of a double sided (DS) T-joint are shown for illustration purposes (Fig. 4a and 4b). Load cases are respectively a normal force F_n ($r_{\sigma s} = 0$) and a combined one involving an additional bending moment M_b ($r_{\sigma s} = 0.25$). Note that at the same time the geometry has changed from approximately a planar ($R_t = 5000$) to a tubular one ($R_t = 36$), implying that the weld notch stress distribution formulations hold in general. The joint dimensions are arbitrary, but realistic for steel maritime structures and the weld notch load carrying level is relatively low: $C_{bw} = \{0.16, 0.15\}$. Comparing the weld toe notch stress and far field stress distributions indicate that equilibrium is satisfied indeed. Converged FE solutions show the accuracy of the formulation.

The bi-linear approximation involves a predefined notch to far field transition location at $0.1(r/t_p)$ and is – in contrast to the semi-analytical formulation (Eqs. 1 and A.1), reflected in C_{bw} – only loading dependent [28], meaning any local notch geometry information is not explicitly taken into account. Note that for $(r/t_p) \to 0$ the notch stress is finite, even for $\rho = 0$; the singular case. If the weld notch load carrying level increases, a notch affected zone size of $0.1(r/t_p)$ turns out to be too small [13,22].

2.1.2. Mode-III formulation

Similar to mode-I, weld toe notch formulations for mode-III are obtained. For non-symmetry with respect to $(t_p/2)$ and $\rho = 0$ [20]:

$$\tau_n\left(\frac{r}{t_p}\right) = \tau_s\left[\tau_{se}\left(\frac{r}{t_p}\right) - 2r_{\tau_s}\left(\frac{r}{t_p}\right)\right] \tag{2}$$

with τ_{se} the self-equilibrium stress part (Appendix A). Formulations are available for symmetry with respect to $(t_p/2)$ as well, including the $\rho > 0$ cases [20].

A non-monotonic and monotonically increasing weld notch stress distribution at the weld toe of a DS T-joint (Fig. 5a and 5b) illustrate the performance of the developed formulations in comparison to the converged FE solutions. The applied load is a torsion moment M_t. Changing the geometry from an approximately planar ($R_t = 5000$) to a tubular one ($R_t = 36$) is responsible for the different structural shear stress ratio, $r_{\tau s} = \{0, 0.25\}$, basically representing an approximately applied shear force F_s load case and a combined one involving an additional torsion moment M_t. In comparison to the mode-I results, for the same geometry the weld notch load carrying level has increased: $C_{tw} = \{0.18, 0.19\}$, as reflected in the increased notch affected region (Figs. 4 and 5).

The bi-linear approximation as originally developed for mode-I has been extended to mode-III applications [27,38–40]. Despite the increased notch affected region, the transition location is still fixed at $0.1(r/t_p)$ and the fit seems not to be perfect. Anyway, even for different C_{tw} values providing a better fit, a predefined and geometry independent transition location remains a modelling limitation for an accurate joint specific weld notch stress distribution representation.

2.2. Weld notch stress intensity distributions

Scaling of welded joint fatigue damage requires a total stress parameter taking all zone {1, 2, 3} contributions into account; a criterion the stress intensity (similarity) factor K seems to meet. Turning the intact geometry related weld toe notch stress distributions into crack damaged equivalents, the zone {1, 2} self-equilibrium and zone 3 equilibrium equivalent stress parts $\{\sigma_{fe}(r/t_p), \sigma_{se}(r/t_p); \tau_{fe}(r/t_p), \tau_{se}(r/t_p)\}$ have been

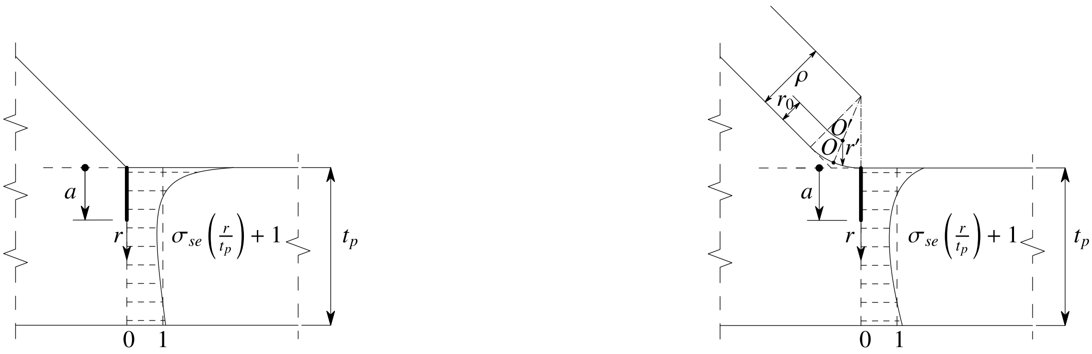

(a) (b)

Fig. 3. Self-equilibrium stress part for a mode-I response applied as unit crack face traction at weld toe notches for $\rho = 0$ (a) and $\rho > 0$ (b).

used to introduce respectively a notch factor $Y_n(a/t_p)$ and a far field factor $Y_f(a/t_p)$, defining the weld toe notch SIF for respectively mode-I and mode-III:

$$K_I \;= \sigma_s\sqrt{t_p}Y_{n,I}(a/t_p)Y_{f,I}(a/t_p)\sqrt{\pi(a/t_p)} \tag{3}$$

$$K_{III} = \tau_s\sqrt{t_p}Y_{n,III}(a/t_p)Y_{f,III}(a/t_p)\sqrt{\pi(a/t_p)}. \tag{4}$$

The stress intensity magnitude is characterised using the structural stress $\{\sigma_s, \tau_s\}$. Assuming the crack tip is infinitely sharp explains the square root behaviour $\sqrt{\pi(a/t_p)}$ for $(a/t_p) \to 0$.

2.2.1. Mode-I formulation

Aiming for a $Y_n Y_f$ rather than $(Y_n + Y_f)$ formulation, $\sigma_{se}(r/t_p)$; the self-equilibrium stress part (Eq. A.1) has been applied as unit crack face traction along the assumed virtual crack path (Fig. 3) using the weight function approach [41]. For non-symmetry with respect to $(t_p/2)$ and $\rho = 0$ [13,22] the notch factor yields (Appendix B):

$$Y_n = \left(\frac{2}{\pi}\right)\int_0^1 \frac{\sigma_{se}\left(\frac{r}{a}\cdot\frac{a}{t_p}\right)+1}{\sqrt{1-\left(\frac{r}{a}\right)^2}}\,\mathrm{d}\left(\frac{r}{a}\right). \tag{5}$$

The linear far field stress distribution $\sigma_{fe}(r/t_p) = \sigma_s\{1 - 2r_{\sigma s}(r/t_p)\}$ in the fracture mechanics context with $\sigma_s = \sigma_{sm} + \sigma_{sb}$ and $r_{\sigma s} = \sigma_{sb}/\sigma_s$ is consistent with the one defined for the welded joint. A superposition of the involved constant membrane and linear bending component applies to the far field factor as well [13,22]:

$$Y_{f,I}\left(\frac{a}{t_b}, r_{\sigma s}\right) = Y_{fm} - r_{\sigma s}(Y_{fm} - Y_{fb}). \tag{6}$$

For a single edge crack configuration in planar structures, $\{Y_{fm}, Y_{fb}\}$ handbook solutions are available [13,22]. For tubular ones new formulations have been established, fitting FE results (Appendix B).

Considering the same geometry and loading conditions as for the weld notch stress distributions (Fig. 4a and 4b), the weld notch stress intensity weight functions $\{Y_{n,I}, Y_{f,I}\}$ are obtained (Fig. 4c and 4d). If the weld notch load carrying level as reflected in C_{bw} is relatively small, $Y_{n,I}$ turns to be governing for $\{0 < (a/t_p) \leq 0.2\}$; a zone {1,2} affected (technical) short crack region, divided into a respectively a notch dominated and a weld load carrying controlled part. Far field factor $Y_{f,I}$ controls the zone 3 contribution in a long-crack region $\{0.2 < (a/t_p) \leq 1\}$, meaning all 3 stress components are decisive in a certain crack length region. Depending on C_{bw} and $r_{\sigma s}$, the $Y_{n,I} - Y_{f,I}$ transition may shift left or right. The FE solutions, obtained for plane strain conditions, proved to be rather good $Y_{n,I}Y_{f,I}$ estimates. Using the bi-linear weld notch stress distribution approximation (Fig. 4a and 4b) to obtain a K_I estimate is one of the traction equivalent structural stress concept features [28,33]; a robust procedure [42]. Although the notch stress intensities are in agreement with the FE solutions (Fig. 4c and 4d) for short cracks, $M_{kn}Y_{f,I}$ seems consistently overestimated for $\{a/(t_p/2)\} < 0.1$. Modifying $Y_{f,I}$ to incorporate the notch characteristic behaviour and establish the notch magnification factor M_{kn} – a Y_n equivalent parameter, rather than adopting the crack face traction definition (Eq. B.1), seems the explanation [22,43]. Differences in the long crack region for the tubular structure (Fig. 4d) are a result of a planar geometry based $Y_{f,I}$ formulation.

The normalised SIF's (K_I/σ_s) for the considered examples perfectly match the FE solution (Fig. 4e and 4f) and hold in general (Fig. 6). Regardless the non-monotonic $Y_{n,I}Y_{f,I}$ behaviour, (K_I/σ_s) remains monotonically increasing because of $\sqrt{\pi(a/t_p)}$ being involved. However, $K_I(M_{kn}Y_{f,I})/\sigma_s$ shows non-monotonic behaviour and includes even a singularity for $(a/t_p) \to 0$. Despite being explained as an higher order effect [28,33], the contribution should be finite at most [44], suggesting fictitious behaviour.

2.2.2. Mode-III formulation

Applying $\tau_{se}(r/t_p)$, the self-equilibrium stress part (Eq. A.2), as unit crack face traction along the assumed virtual crack path using the weight function approach [41] provides for non-symmetry with respect to $(t_p/2)$ and $\rho = 0$ (Appendix C):

$$Y_n = \left(\frac{2}{\pi}\right)\int_0^1 \frac{\tau_{se}\left(\frac{r}{a}\cdot\frac{a}{t_p}\right)}{\sqrt{1-\left(\frac{r}{a}\right)^2}}\,\mathrm{d}\left(\frac{r}{a}\right). \tag{7}$$

Similar formulations are obtained for symmetry with respect to $(t_p/2)$ and $\rho > 0$ (Appendix C). The far field stress distribution $\tau_{fe}(r/t_p) = \tau_s\{1 - 2r_{\tau s}(r/t_p)\}$ with $\tau_s = \tau_{ss} + \tau_{st}$ and $r_{\tau s} = \tau_{st}/\tau_s$ involves a superposition of a constant shear force and linear torsion moment induced component and applies principally to the far field factor as well:

$$Y_{f,III}\left(\frac{a}{t_b}, r_{\tau s}\right) = Y_{fs} - r_{\tau s}(Y_{fs} - Y_{ft}) \tag{8}$$

with structural shear stress ratio $r_{\tau s} = t_b/(2R_t)$ and $\{Y_{fs}, Y_{ft}\}$ either obtained from handbook solution or derived (Appendix C).

For the same geometry and loading conditions, the increased weld notch stress affected region for mode-III in comparison to mode-I translates (Figs. 4 and 5a and 5b) one-to-one to the $Y_{n,III}Y_{f,III}$ distribution (Figs. 4 and 5c and 5d). The $Y_{n,III}$ controlled zone {1,2} short crack region has increased to $\{0 < (a/t_p) \leq 0.3\}$, meaning the $Y_{f,III}$ defined zone 3 long-crack region has decreased to $\{0.3 < (a/t_p) \leq 1\}$. Different

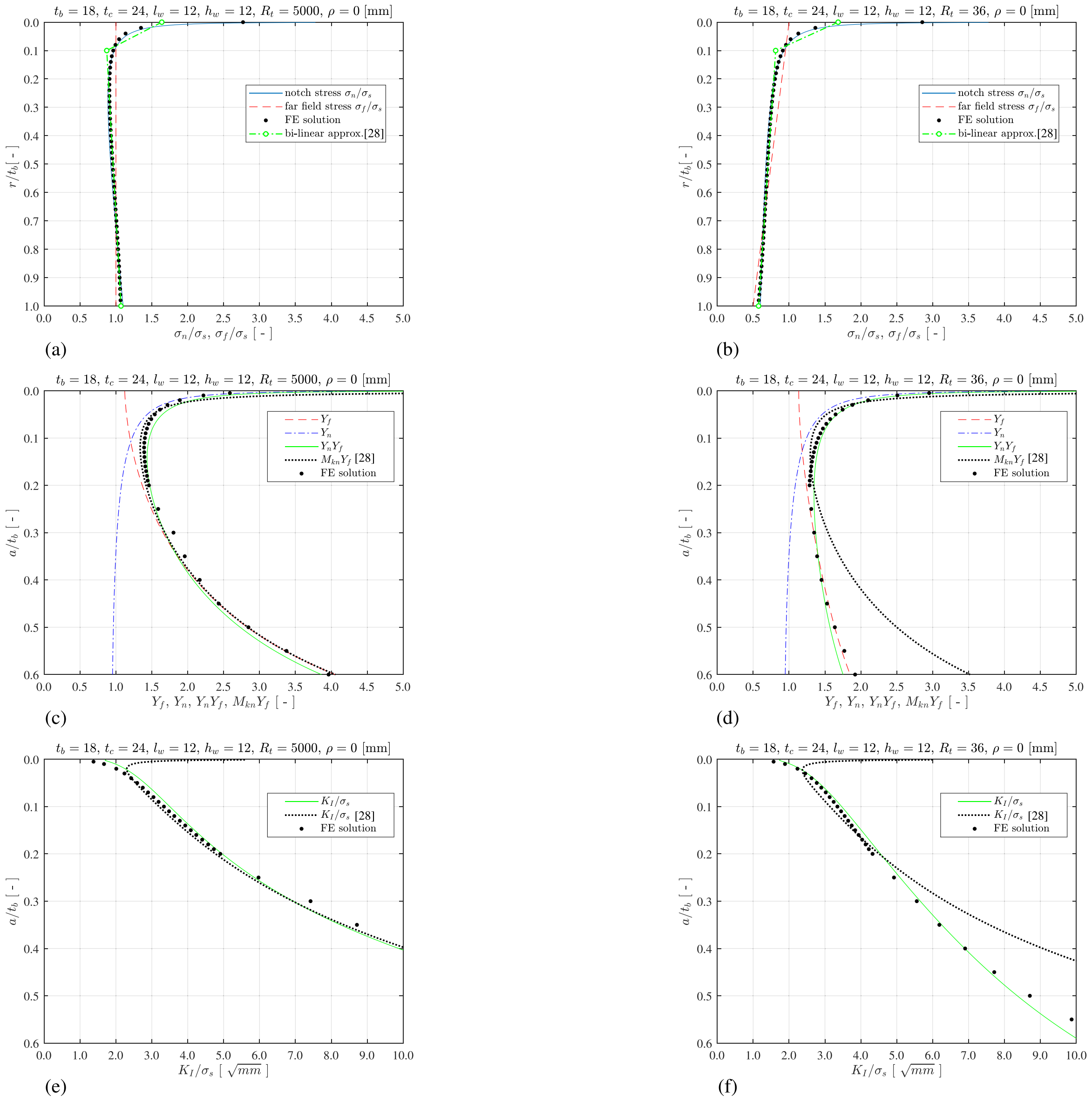

Fig. 4. Mode-I weld toe notch stress distribution (a, b), SIF far field- and notch distribution (c, d) and K_I distribution (e, f) for a DS welded T-joint; $r_{\sigma_s} = 0$ (a, c, e), $r_{\sigma_s} = 0.25$ (b, d, f).

C_{tw} and $r_{\tau s}$ values shift the $Y_{n,III} - Y_{f,III}$ transition left or right. A good agreement with FE solutions is obtained.

Assuming the mode-{I, III} weld notch stress distribution characteristics are similar, the bi-linear approximation – including the transition location at $0.1(r/t_p)$ – does not change and the traction equivalent structural stress concept $M_{kn}(a/t_p)$ formulation is pretended to be the same as well. Handbook solutions are used to define the far field factor $Y_{f,III}$ [27]. However, comparing the mode-{I, III} results (Figs. 4 and 5c and 5d), the notch stress intensity has turned from a small $M_{kn}Y_{f,I}$ – into a significant $M_{kn}Y_{f,III}$ overestimate. Whereas for the stress distribution the transition location should change to a larger value, reflecting an enlarged short crack region, a smaller – contradictory – one seems required to provide a better intensity estimate; a consequence of the M_{kn} definition [13,22,28]. The overestimates in the long crack region are a consequence of the solid shaft $Y_{f,III}$ solution, being insufficient for hollow shafts; tubular structures, or even planar ones. Adopting $Y_{f,III}$ (Eq. 8) improves the far field estimate.

The (K_{III}/τ_s) solutions for the considered examples perfectly match the FE results (Fig. 5e and 5f), and hold in general (Fig. 6). Fictitious non-monotonic $K_{III}(M_{kn}Y_{f,III})/\tau_s$ behaviour for $\{(a/t_p) \to 0\}$ is observed up to a relatively large extent in comparison to the mode-I results, in particular for an unchanged transition location at $0.1(r/t_p)$.

3. Total stress assessment

For mixed mode-{I, III} multiaxial response conditions of planar and tubular maritime structures, the mode-I contribution is governing, meaning the normal stress is predominant (Section 1). At the same time, the fatigue lifetime of arc-welded joints is growth – rather than shear induced initiation – controlled because of the welding induced defects, explaining why a cracked geometry based fatigue strength parameter will be adopted to establish a normal stress equivalent von Mises type of failure criterion [21]. Involving the stress intensity distributions at the critical fracture plane (Section 2), the total stress parameter $S = S_T = \sqrt{S_{T,I}^2 + \beta(N) S_{T,III}^2}$ will be established first (Section 3.1), including a lifetime dependent shear stress coefficient $\beta(N)$. Cycles will be counted – because of the time domain approach – in the von Mises plane, in order to be able to incorporate non-proportionality cycle-by-cycle. The linear damage accumulation model will be used, since

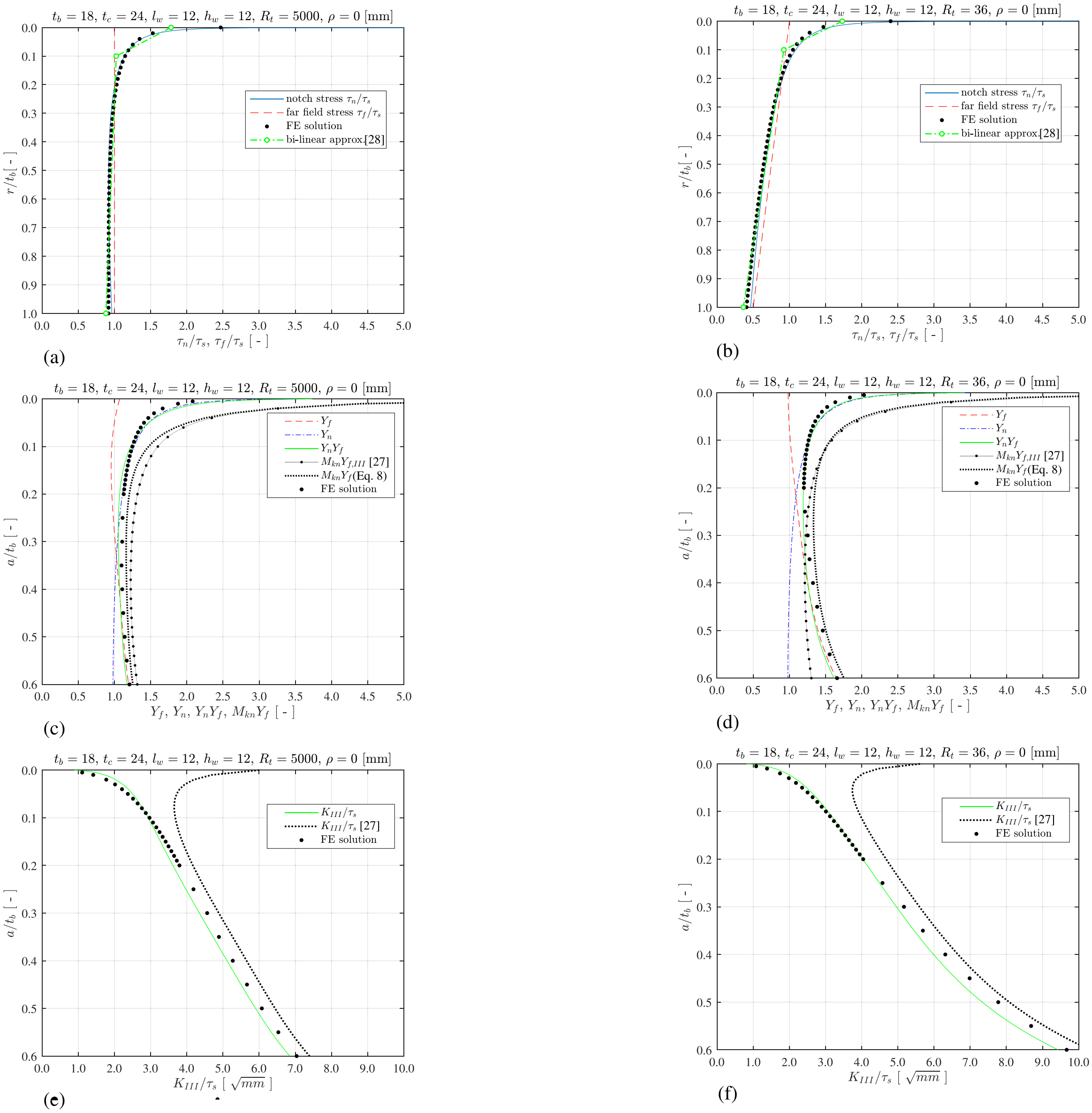

Fig. 5. Mode-III weld toe notch stress distribution (a, b), SIF far field- and notch distribution (c, d) and K_{III} distribution (e, f) for a DS welded T-joint; $r_{\tau_s} = 0$ (a, c, e), $r_{\tau_s} = 0.25$ (b, d, f).

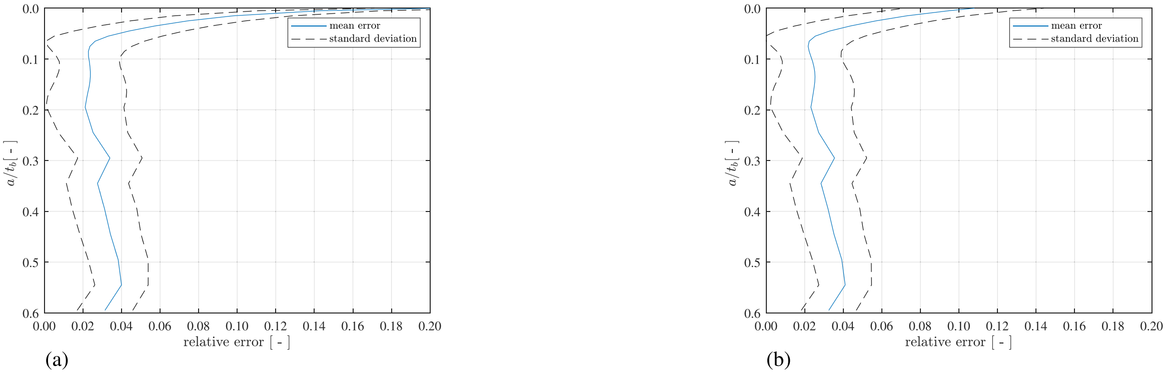

Fig. 6. Relative K_I (a) and K_{III} (b) error for DS welded T-joint, comparing the FE solutions and the analytical results for the full parameter application range.

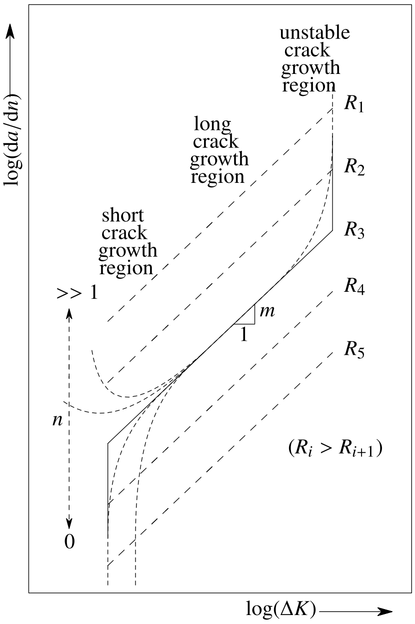

Fig. 7. Elastoplasticity and mean stress effects in the short and long crack growth region.

good performance has been shown for advanced fatigue strength criteria [22]. Using mid-cycle fatigue test data from literature (Section 3.2) the strength and mechanism contributions, reflected in respectively mode specific $\{\log(C), \gamma\}$ and $\{m, n\}$ coefficients, will be investigated (Section 3.3).

3.1. Fatigue strength parameter

Cyclic loading induced response conditions turn the SIF's $\{K_I, K_{III}\}$ into crack growth driving forces $\{\Delta K_I, \Delta K_{III}\}$ and defects may develop into cracks. The crack growth rate $(\mathrm{d}a/\mathrm{d}n)$ of short-cracks emanating at notches show elastoplastic wake field affected anomalies [22]. Modifying Paris' equation, a generalised two-stage model has been established containing a transition; a natural pivot rather than a mathematical one [45,46] from a short to a long crack growth region meant to incorporate all relevant crack growth driving force components [47–49]; i.e. to include both the weld notch- and far field characteristic mode-I response contributions: $(\mathrm{d}a/\mathrm{d}n)_I = C_I \cdot Y_{n,I}^{n_I} \cdot \{\Delta\sigma_{s,eff} \cdot Y_{f,I} \cdot \sqrt{(\pi a)}\}^{m_I}$. Notch elastoplasticity coefficient n_I is response dependent and defines the level of monotonically increasing or non-monotonic crack growth behaviour (Fig. 7), in contrast to a fixed value in a similar model: $(\mathrm{d}a/\mathrm{d}n)'_I = C \cdot M_{kn}^n \cdot \{\Delta\sigma_{s,eff'} \cdot Y_{f,I} \cdot \sqrt{(\pi a)}\}^m$ with $n = 2$, assuming response invariant non-monotonic behaviour [10,28,50,51]. Since welding induced residual stress affects n_I, as-welded (AW) joint fatigue resistance data is typically used to obtain an average estimate, rather than crack growth data obtained using standard specimens geometries like the compact tension configuration [11]. Recognising that a spatial description of a loading induced response cycle requires two parameters, e.g. range $\Delta\sigma_s$ and ratio $R_I = (\sigma_{s,min}/\sigma_{s,max})$ reflecting a mean stress effect, Walker's model has been adopted [11,13,52]. The stress range becomes an effective one: $\Delta\sigma_{s,eff} = \Delta\sigma_s/\{(1-R_I)\}^{1-\gamma}$ with $0 \leq \gamma \leq 1$. For $\gamma \to 1$, the nominal stress range $\Delta\sigma_s$ dominates the fatigue resistance; the mean stress becomes governing for $\gamma \to 0$. Assuming mean stress affects predominantly the notch region [50,51], $\Delta\sigma_{s,eff'} = \Delta\sigma_s/\{(1-R_I)\}^{n(1-\gamma)/m}$. Mean stress coefficient $\gamma = 0.5$ for $R_\sigma \leq 0$ and reflects an equal contribution of the stress range $\Delta\sigma_s$ and max stress $\sigma_{s,max} = \Delta\sigma_s/(1-R_I)$; $\gamma = 0$ for $R_\sigma < 0$ meaning only $\Delta\sigma_s^+$ is considered to contribute effectively. Incorporating the welding induced residual (mean) stress distribution as well – if available, a different interpretation seems to apply and R_I turned into a crack length dependent far field stress intensity contribution: $\Delta\sigma_{s,eff'} = \Delta\sigma_s/\{1 - R_{Ir}(a/t_p)\}^{1-\gamma}$ with $R_{Ir}(a/t_p) = [K_I(\sigma_{s,max}, a/t_p) + K_I\{\sigma_r(a/t_p), a/t_p\}]/[K_I(\sigma_{s,min}, a/t_p) + K_I\{\sigma_r(a/t_p), a/t_p\}]$ and $\gamma = 0.5$ for any $R_{Ir}(a/t_p)$ [53].

Crack growth behaviour at notches for a mode-III response as often observed is monotonically increasing [54–60]. However, some evidence for non-monotonic crack growth is available as well [61–63], principally justifying a mode-I model similarity: $(\mathrm{d}a/\mathrm{d}n)_{III} = C_{III} \cdot Y_{n,III}^{n_{III}} \cdot \{\Delta\tau_{s,eff} \cdot Y_{f,III} \cdot \sqrt{(\pi a)}\}^{m_{III}}$. Non-monotonicity becomes more pronounced for a small notch radius ($\rho \to 0$), a large amplitude – negative ratio characterised response $\{\tau_s \to \tau_y, R_{III} < 0\}$ and a plane stress condition, supporting large scale yielding [22].

For crack growth in mixed mode-{I, III} conditions an equivalent stress intensity can be adopted, typically similar to equivalent stress formulations [21], either a linear one of the Tresca type: $\Delta K_{eq} = C_I \cdot K_I + C_{III} \cdot K_{III}$ or a non-linear one of the von Mises type: $\Delta K_{eq} = \sqrt{(C_I \cdot K_I)^2 + (C_{III} \cdot K_{III})^2}$ [40,57–60,63–71]. Even higher order non-linear formulations have been proposed and some contain coupling terms to incorporate interaction effects [40,70,71]. However, because of the $S_{eq} - \Delta K_{eq}$ formulation similarity, an equivalent stress S_{eq} [21] rather than an equivalent stress intensity ΔK_{eq} will be adopted as fatigue strength parameter, aiming for a mixed mode-{I, III} $S_{eq} - N$ fatigue resistance – rather than a $\Delta K_{eq} - (\mathrm{d}a/\mathrm{d}n)$ crack growth relation.

Applying an integral operator on the individual mode-{I, III} crack growth models provides mid-cycle fatigue related resistance relations of the Basquin type: $\log(N_j) = \log(C_j) - m_j \log(S_{T,j})$ with j ={I, III}, correlating the fatigue life time N_i and a total stress fatigue strength parameter [10,11,13,22]:

$$S_{T,j} = \frac{S_j}{\left(1 - R_j\right)^{1-\gamma} \cdot I_{N,j}^{\frac{1}{m_j}} \cdot t_p^{\frac{2-m_j}{2m_j}}} \tag{9}$$

with

$$I_{N,j} = \int_{\frac{a_i}{t_p}}^{\frac{a_f}{t_p}} \frac{1}{\left\{Y_{n,j}\left(\frac{a}{t_p}\right)\right\}_j^n \cdot \left\{Y_{f,j}\left(\frac{a}{t_p}\right)\right\}_j^m \cdot \left(\frac{a}{t_p}\right)^{\frac{m_j}{2}}} \mathrm{d}\left(\frac{a}{t_p}\right),$$

$S_I = \Delta\sigma_s$ and $S_{III} = \Delta\tau_s$. Scaling parameter $t_p^{(2-m_j)/2m_j}$ takes the response gradient induced size effects into account. Rather than a sufficiently small (a_i/t_p) providing a converged notch crack growth integral solution $I_{N,j}$, an arc-welding induced most likely material characteristic defect size estimate has been established; $(a_f/t_p) = 1$ is based on a through-thickness crack criterion.

An environment and service loading induced mean stress component as reflected in $\{R_I, R_{III}\}$ is in general not the only one, since arc-welding adds a thermal loading induced – typically high-tensile – quasi-constant residual (mean) stress, affecting the fatigue strength. An explicit residual stress measure is typically not included, since for fatigue design in general only joints in AW condition are considered [34,44,72], meaning any residual stress affecting the fatigue resistance is just implicitly incorporated in the most likely fatigue resistance parameter estimates. A stress relieving heat treatment can be applied, being one way to virtually eliminate residual stress and improve the fatigue strength. If both AW and stress-relieved (SR) test data are jointly considered, an explicit residual stress measure S_r – an average estimate, since the actual distribution is typically unknown – will be introduced to represent the thermal condition, meaning a re-formulation of the response ratio is required:

$$R_{Ir} = \frac{S_{T,I,min} + S_r}{S_{T,I,max} + S_r} = \frac{R_I \cdot S_{T,I} + S_r(1-R_I)}{S_{T,I} + S_r(1-R_I)} \tag{10}$$

$$R_{IIIr} = \frac{S_{T,III,min} + S_r}{S_{T,III,max} + S_r} = \frac{R_{III} \cdot S_{T,III} + S_r(1-R_{III})}{S_{T,III} + S_r(1-R_{III})}. \tag{11}$$

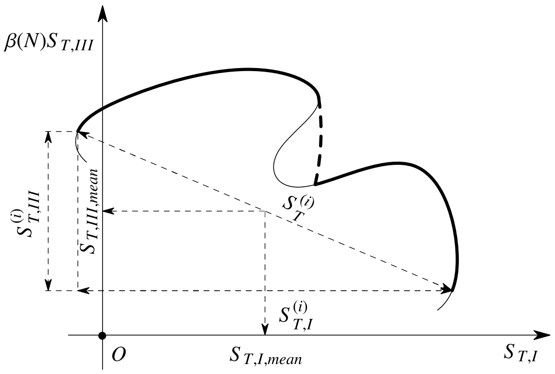

Fig. 8. Total stress cycle characteristics in the von Mises plane.

Since a stress relieving heat treatment affects the grain size and local yielding properties [21], a dedicated elastoplasticity coefficient n will be needed for the AW and SR conditions.

Because of the mode-I and mode-III finite life time specific strength and mechanism fatigue resistance characteristics, a response level dependent shear strength coefficient $\beta(N)$ – rather than a constant one – can be defined for a single-slope resistance relation $N = C \cdot S_T^m$ in the mid-cycle fatigue region [21]:

$$\beta(N) = \frac{S_{T,I}(N)}{S_{T,III}(N)} = C_\beta \cdot N^{M_\beta} \tag{12}$$

with

$$C_\beta = 10^{\frac{\log(C_I) m_{III} - \log(C_{III}) m_I}{m_I \cdot m_{III}}}$$

and

$$M_\beta = \frac{m_I - m_{III}}{m_I \cdot m_{III}}.$$

Since only the uniaxial mode-{I, III} number of cycles $\{N_I, N_{III}\}$ are known in advance, the actual $\beta(N)$ value has to be obtained in an iterative cycle counting process [21] in order to capture N for the equivalent normal stress based von Mises type of criterion:

$$S_T = \sqrt{\left\{ S_{T,I}^2 + \beta(N) \cdot S_{T,III}^2 \right\}}. \tag{13}$$

Counting iteratively the effective von Mises notch stress (Fig. 8) at the critical fracture plane (Section 2), the range $S_{T,i}$ including the normal and equivalent shear stress projections $\{S_{T,I,i}, \beta(N) \cdot S_{T,III,i}\}$ and corresponding ratios $\{R_I = S_{T,I,min,i}/S_{T,I,max,i}, R_{III} = \beta(N) \cdot S_{T,III,min,i}/\beta(N) \cdot S_{T,III,max,i}\}$ can be obtained for each cycle i. Adopting a 0^{th}, 1^{st} or 2^{nd} order moment approach, differences between the actual response path and the (straight) range have been used to incorporate a non-proportionality effect cycle-by-cycle in terms of C_{np}, including a material characteristic contribution in terms of c_m [21,39,73–75]:

$$S_{T,eff,i} = S_{T,i}\left(1 + c_m \cdot C_{np,i}\right) \tag{14}$$

with

$$C_{np,i} = \frac{\int_{\widetilde{S}} (r \cdot |\sin(\theta)|)^n \mathrm{d}p}{\int_S (R \cdot |\sin(\theta)|)^n \mathrm{d}p} \qquad \text{for} \quad n = 0, 1 \text{ or } 2. \tag{15}$$

Although $C_{np,i}$ and c_m are meant to reflect respectively the path and material characteristic part, c_m may correct for any cycle counting and/or non-proportionality related model deficiency as well, since data fitting is used to obtain an estimate. A compromised value may be acquired, meaning interpretation becomes more difficult. In order to obtain a mid-cycle fatigue related equivalent total stress parameter $S_{T,eq}$ for variable amplitude (VA) data fitting the constant amplitude (CA) data scatter band; i.e. $N(S_T) = C \cdot S_T^{-m}$ with $S_T = S_{T,eq}$, the linear damage model is adopted: $D = \sum\{n_i(S_{T,i})/N_i(S_{T,i})\} \leq 1$ with $N_i(S_{T,i}) = C \cdot S_{T,i}^{-m}$. For $D = 1$, reflecting failure, the formulation becomes:

$$S_{T,eq} = \left[\frac{\sum\{n_i(S_{T,eff,i}) \cdot S_{T,eff,i}^m\}}{N} \right]^{1/m}. \tag{16}$$

Similarly, applying an integral operator to the $(\mathrm{d}a/\mathrm{d}n)_{I'} = C \cdot M_{kn}^2 \cdot \{\Delta\sigma_{s,eff'} \cdot Y_{f,I} \cdot \sqrt{(\pi a)}\}^m$ mode-I crack growth relation [28,50,51] provides a master curve formulation: $\log(N_I) = \log(C_I) - m_I \log(S_{t,I})$ with $S_{t,I} = \Delta\sigma_s/\{(1-R_\sigma)^{2(1-\gamma)/m} \cdot I_{N,I'}(r_{\sigma s})^{1/m_I} \cdot t_p^{(2-m_I)/2m_I}\}$. The crack growth integral $I_{N,I'}(r_{\sigma s})^{1/m_I} = [\int 1/M_{kn}^2(a/t_p) \cdot Y_{f,I}(a/t_p, r_{\sigma s})^{m_I} \cdot (a/t_p)^{m_I/2} \mathrm{d}(a/t_p)]^{(1/m_I)}$ is approximated using a 6^{th} order polynomial for engineering purposes [25]. Provided $r_{\sigma s} = |\Delta\sigma_{sb}|/(|\Delta\sigma_{sm}| + |\Delta\sigma_{sb}|)$ [25,76,77], non-monotonic weld notch stress distributions [11,13] are not considered since the formulation provides only $r_{\sigma s} \geq 0$ values. Because of the fixed notch governing to far field dominated transition location, the considered weld notch load carrying level is the same for all. Rather than an arc-welding induced most likely material characteristic defect size estimate, $(a_i/t_p) = 10^{-3}$ has been adopted providing a converged $I_{N,I'}(r_{\sigma s})^{1/m_I}$ solution; $(a_f/t_p) = 1$ is based on a through-thickness crack criterion. Whereas for SR welded joints in steel structures $\Delta\sigma_{s,eff'}$ is considered, for AW ones mean stress effects are not taken into account and $\Delta\sigma_{s,eff'} \rightarrow \Delta\sigma_s$, reducing the mode-I traction equivalent structural stress to $S_{t,I} = \Delta\sigma_s/\{I_{N,I'}(r_{\sigma s})^{1/m} \cdot t_p^{(2-m)/2m}\}$ [25,40].

Mode-III crack growth at notched geometries seems not investigated. However, a traction equivalent structural shear stress formulation has been established, assuming the non-monotonic behaviour as identified for mode-I still holds: $S_{t,III} = \Delta\tau_s/\{I_{N,III'}(r_{\tau s})^{1/m_{III}} \cdot t_p^{(2-m_{III})/2m_{III}}\}$. A 4^{th} order polynomial has been established [27,38] to approximate the notch crack growth integral $I_{N,III'}(r_{\tau s})^{1/m_{III}} = [\int 1/\{M_{kn}^2(a/t_p) \cdot Y_{f,III}(a/t_p, r_{\tau s})^{m_{III}} \cdot (a/t_p)^{m_{III}/2} \mathrm{d}(a/t_p)\}]^{1/m_{III}}$ involving the solid shaft $Y_{f,III}$ solution (Section 2.2.2) [27,38] and is applicable for monotonic weld notch shear stress distributions only: $r_{\tau s} = |\Delta\tau_{st}|/(|\Delta\tau_{ss}| + |\Delta\tau_{st}|)$. Slope $m_{III} = 5$ has been postulated. Using the improved far field factor $Y_{f,III}$ formulation (Eq. 8), $I_{N,III'}(r_{\tau s})^{1/m_{III}}$ has been re-established and a revised polynomial approximation is proposed. The notch characteristics (Section 2) have not been changed, meaning the transition size is assumed to be the same as for mode-I.

For mixed mode-{I, III} multiaxial fatigue, a von Mises type of equivalent stress formulation has been adopted, defined at the critical fracture plane (Section 2):

$$S_t = \sqrt{(S_{t,I}^2 + \beta \cdot S_{t,III}^2)} \tag{17}$$

with

$$S_{t,I} = \Delta\sigma_s / \left\{ (1 - R_\sigma)^{2(1-\gamma)/m} \cdot I_{N,I'}(r_{\sigma s})^{1/m_I} \cdot t_p^{(2-m_I)/2m_I} \right\}$$

$$\begin{aligned} I_{N,I'}(r_{\sigma s})^{1/m_I} \approx\; & 0.0011 \cdot r_{\sigma s}^6 + 0.0767 \cdot r_{\sigma s}^5 - 0.0988 \cdot r_{\sigma s}^4 + \\ & 0.0946 \cdot r_{\sigma s}^3 + 0.0221 \cdot r_{\sigma s}^2 + 0.014 \cdot r_{\sigma s} + 1.2223 \end{aligned}$$

$$S_{t,III} = \Delta\tau_s / I_{N,III'}(r_{\tau s})^{1/m_{III}} \cdot t_p^{(2-m_{III})/2m_{III}}$$

$$\begin{aligned} I_{N,III'}(r_{\tau s})^{1/m_{III}} \approx\; & 1.4131 \cdot r_{\tau s}^4 - 1.0448 \cdot r_{\tau s}^3 + \\ & 1.0264 \cdot r_{\tau s}^2 + 0.7087 \cdot r_{\tau s} + 1.4244 \end{aligned}$$

and $\beta = 3$; a constant rather than a response level dependent one, explaining why fatigue resistance data analysis for welded joints in steel structures provided an average slope value $m \sim 4$ [27,39,78,79] in between $m_I \sim 3$ and $m_{III} \sim 5$. Another track has been developed as well. Because well-established mode-III short and long crack growth data is lacking, $S_t = \Delta\sigma_{s,vM}/\{I_{N,I'}(r_{s,vM})^{1/m_I} \cdot t_p^{(2-m_I)/2m_I}\}$ with $\Delta\sigma_{s,vM} = \sqrt{(\Delta\sigma_s^2 + \beta \cdot \Delta\tau_s^2)}$, $r_{s,vM} = \sqrt{(\Delta\sigma_{sb}^2 + \beta \cdot \Delta\tau_{st}^2)}/\{\sqrt{(\Delta\sigma_{sm}^2 + \beta \cdot \Delta\tau_{ss}^2)} + |\Delta\sigma_{sb}|\}$ and $\beta = 3$ has been proposed, assuming the crack growth behaviour is mode-I dominated [26,40]. If mode-III contributions become more important, deviations can be expected.

Cycles are counted in the $S_{t,I} - \beta S_{t,III}$ or $\sigma_s - \beta\tau_s$ plane [26,27,39,40] for the proposed S_t formulations – respectively incorporating

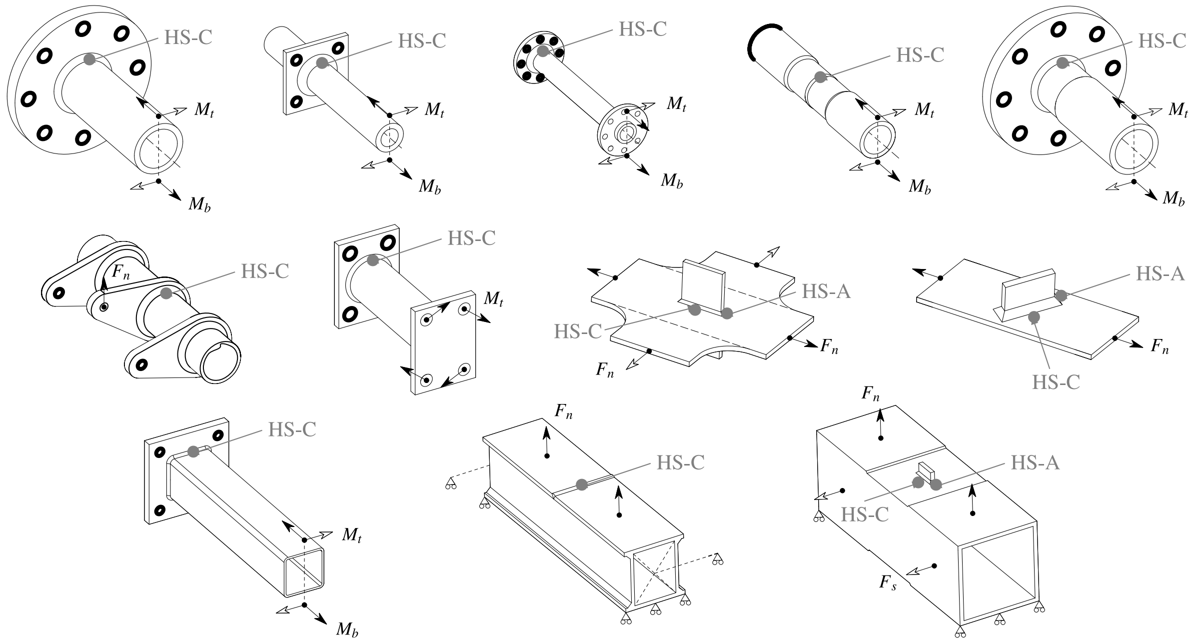

Fig. 9. Fatigue test specimen geometry, external loading (arrows) and constraints (thick lines or △ symbols) [21].

full- or just partial far field fatigue strength information and includes cycle-by-cycle non-proportionality measures [39,73–75].

In order to obtain an equivalent stress parameter $S_{t,eq}$ for VA data fitting the CA data scatter band, the linear damage model is adopted: $D = \sum\{n_i(S_{t,i}) \cdot S^m_{t,i}/N_i(S_{t,i})\}$. For $D = 1$, the formulation becomes: $S_{t,eq} = [\sum\{n_i(S_{t,i})/N\}]^{1/m}$ with $N = \sum\{n_i(S_{t,i})\}$ the total number of counted von Mises cycles.

3.2. Test data

Data series containing steel specimens with both tubular and planar structural joints have been considered (Fig. 9) – the same as used to investigate the effective notch stress performance [21], involving respectively circular/square hollow and plate cross-sections with specified joint dimensions and various thermal conditions (both AW and SR).

3.3. Strength and mechanism contributions

The life time range of the considered data (Fig. 9) virtually reflects mid-cycle fatigue characteristics only: $N = (10^4 \sim 5 \cdot 10^6)$ cycles. A log–log linear resistance formulation of the Basquin type typically relates N to a fatigue strength parameter S [11]: $\log(N) = \log(C) - m \cdot \log(S)$. Linear regression on life time is adopted to estimate the single-slope curve parameters: intercept $\log(C)$ and slope m, respectively reflecting a strength and mechanism contribution, introducing the life time scatter (i.e. performance) parameter σ_N. For strength performance evaluation purposes, the scatter band index $T_{\sigma S} = 1 : (S_{10}/S_{90})$ will be used: the fatigue strength ratio for 10[%] and 90[%] probability of survival [80]. Maximum likelihood based regression [22,81] will be employed to obtain the most likely parameter vector estimate Φ : $\max \mathcal{L}(\Phi; N|S)$ with $\Phi = \{\log(C), m, \sigma_N\}$, assuming fatigue lifetime N is most likely log-Normal distributed [13,20]. For $S = S_{T,eff}$ (Section 3.1), the response ratio coefficient and material characteristic elastoplasticity coefficient providing respectively another strength and mechanism contribution are introduced, principally extending the parameter vector to: $\Phi = \{\log(C), \gamma, m, n, \sigma_N\}$. Note that ideally the uniaxial mode-I and mode-III, as well as the multiaxial P and NP mode-{I, III} data (Fig. 9) would have been balanced for appropriate $S_{T,eff}$ performance evaluation, meaning that except the σ_N and $T_{\sigma S}$ parameters as global indicators for all data, the individual data groups behaviour have to be carefully considered as well. Starting with the uniaxial reference fatigue resistance in terms of $S_{T,eff}$, the mode specific strength and mechanism coefficients will be established first (Section 3.3.1) in order to obtain $\beta(N)$. The $S_{T,eff}$ performance for multiaxial fatigue resistance data will be investigated accordingly (Section 3.3.2), in comparison to $S_{e,eff}$ and S_t. Particular attention will be paid to the consequences of mode specific strength and mechanism for mixed mode-{I, III} fatigue and the influence of non-proportionality. Since $S_{T,eff}$ is an equivalent normal stress von Mises type of parameter, the fitting of the multiaxial data in the mode-I uniaxial data scatter band will be verified, as well as the fitting of VA data in the CA data scatter band in order to establish the performance of the adopted linear damage accumulation model for a $S_{T,eff}$ based fatigue assessment.

3.3.1. Uniaxial reference fatigue data

The $S_{T,eff}$ based mode-I mid-cycle fatigue resistance formulation for planar structures in steel (maritime) structures, involving hot spots type {A, B, C} and various AW joint geometries, has already been established for CA data [43] and shows excellent performance as reflected in the life time standard deviation: $\sigma_N = 0.21$. The intercept and slope as strength and mechanism parameters are: $\log(C_I) \sim 13.05$ and slope $m_I \sim 3.15$. Note that the slope is close to the typical design value $m = 3$ [34,72]. Response ratio coefficient $\gamma_{I,AW} \sim 0.89$ for the full R_I range implies a predominant contribution of stress range over mean stress. For an average most likely initial crack size $(a_i/t_p) = 0.006$ and final crack size $(a_f/t_p) = 1$ – representing a through-thickness crack (Section 2) – and real notch radius $\rho = 0$ (Fig. 7), a most likely $n_{I,AW} \sim 3.48$ has been obtained, reflecting notch and/or crack tip elastoplasticity induced non-monotonic crack growth behaviour (Fig. 7). Both $\gamma_{I,AW}$ and $n_{I,AW}$ are welding induced high-tensile residual stress affected. Since the data size of the considered (predominant) tubular and (some) planar mode-I data (Fig. 9) is ~ 140, relatively small in comparison to the ~ 2500 assessed before [43], enforcing $\log(C_I) \sim$

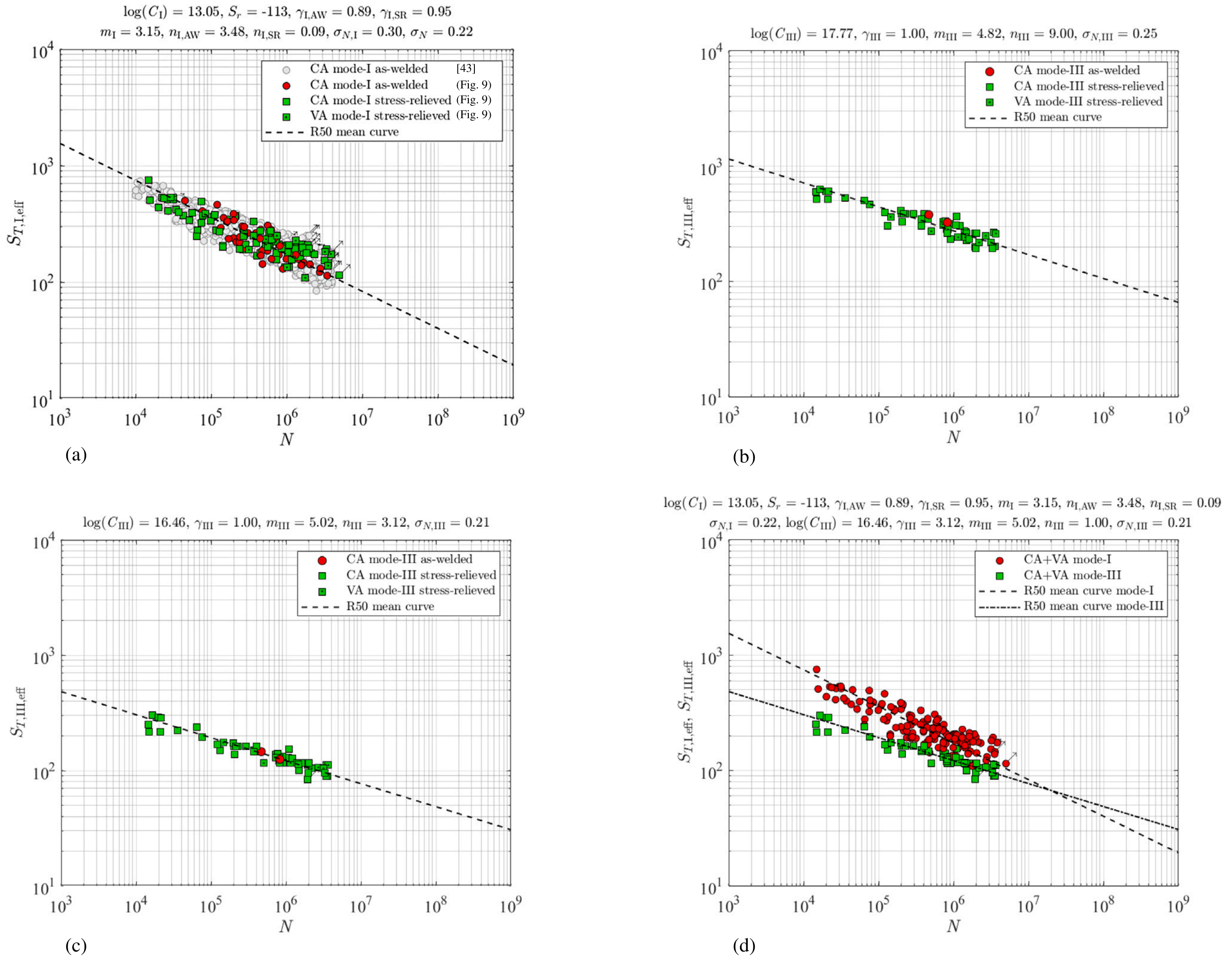

Fig. 10. Uniaxial reference fatigue resistance. Mode-I data total stress based fatigue resistance, including mean and residual stress correction with dedicated $n_{I,AW}$ and $n_{I,SR}$ (a); Mode-III data total stress based fatigue resistance; $\rho = 0$ (b) and $\rho > 0$ (c). Uniaxial mode-I and mode-III data total stress based fatigue resistance (d). Note: $c_m = C_{np,i} = 0$.

Table 1
Total stress based parameter estimates and 75[%] lower and upper parameter confidence bounds for mode-I and mode-III.

Parameter	Mode-I		Mode-III			
			$\rho = 0$		$\rho > 0$	
log(C)	13.05	[12.97, 13.13]	17.77	[17.11, 18.43]	16.46	[15.90, 17.02]
m	3.15	[3.11, 3.18]	4.82	[4.46, 5.18]	5.02	[4.67, 5.37]
n	/	/	9.00	[4.17, 13.83]	3.12	[1.14, 5.09]
n_{AW}	3.48	[3.28, 3.68]	/	/	/	/
n_{SR}	0.09	[0.01 0.17]	/	/	/	/
γ	/	/	1.00	[0.98, 1.00]	1.00	[0.98, 1.00]
γ_{AW}	0.89	[0.88, 0.91]	/	/	/	/
γ_{SR}	0.95	[0.93, 0.98]	/	/	/	/
S_r	−113	[−115, −110]	/	/	/	/
σ_N	0.30	[0.26, 0.33]	0.25	[0.22, 0.28]	0.21	[0.18, 0.24]
σ_N incl.[43]	0.22	[0.19, 0.24]	/	/	/	/

13.05, $m_I \sim 3.15$, $\gamma_{I,AW} \sim 0.89$ and $n_{I,AW} \sim 3.48$ seems straightforward from parameter confidence perspective. A previous fatigue resistance investigation based on the effective notch stress S_e [21]; an intact geometry fatigue strength parameter, revealed that distinguished material dependent strength and mechanism contributions for AW and SR thermal conditions are required, suggesting dedicated $\{\gamma_{I,SR}, n_{I,SR}\}$ estimates should be assigned. At the same time, an explicit residual stress measure S_r is introduced for the SR data since AW and SR data are jointly considered, meaning the response ratio R_{I_r} rather than R_I should be adopted (Section 3.1). The parameter vector becomes: $\Phi = \{S_{r,I}, \gamma_{I,SR}, n_{I,SR}, \sigma_{N,I}\}$. Regression analysis shows that the AW and SR data (Fig. 9) fit the reference AW data scatter band (Fig. 10), suggesting strength and mechanism contributions are sufficiently covered. The most likely residual stress estimate S_r (Fig. 10 and Table 1) proved to be compressive (Section 3.1), confirming the (average) residual stress for the AW data is highly tensile indeed. Note $S_{r,I}$ is a total stress rather than a structural stress value (Section 3.1), meaning a one-to-one comparison to the S_e based $S_{r,I}$ value [21] is not possible. Surprisingly, the residual mean stress coefficient $\gamma_{I,SR}$ has become about equal to the AW value $\gamma_{I,AW}$ – although for the S_e based fatigue resistance assessment the same behaviour is observed, meaning the stress range contribution dominates anyway. The $n_{I,SR} \sim 0.09$ estimate (Fig. 10 and Table 1) turns out to be smaller than the AW value as expected and reflects soft monotonically increasing crack growth behaviour (Fig. 7) – close to log–log-linear behaviour in the Paris defined long-crack growth region and correlates to a predominant elastic notch and/or crack tip response as a consequence of eliminated residual (mean) stress. At the same time, a stress-relieving heat treatment decreases the hardness and supports ductile material behaviour, improving the elastic material capacity. However, since the amount of SR data is just ∼ 3 [%] of the total size, data balance is lost, meaning $n_{I,SR}$ is likely compromised up to some extent in order to enforce an AW data fit. The life time scatter of the considered data (Fig. 9) in terms of $\sigma_{N,I}$ is somewhat large and seems at least partially a matter of data size as reflected in the parameter confidence (Table 1). The corresponding strength scatter band index $T_{\sigma S_T} = 1 : 1.77$ and turns out to be larger than a typical value of $1 : 1.50$ [15]. In comparison to S_e [21], the S_T performance is slightly worse.

At first glance, the VA data fits the CA data scatter band for $D = 1$, supporting the hypothesis that advanced fatigue damage criteria – including the mean stress as an important sequence parameter in terms of R and γ – contributes to the (linear) damage accumulation model performance.

The mode-III mid-cycle fatigue resistance for (predominantly) tubular steel (maritime) structures principally involves hot spots type C and a DS welded T-joint geometry only (Fig. 9). The data size is ~ 50. Since the (as) weld(ed) toe notch radius is a stochastic variable along the weld seam and quite small [82], $\rho = 0$ is typically adopted. However, S_e based investigations [21] suggest that the actual ρ value is important, explaining why regression analysis will be performed for the $\rho > 0$ case. For reference purposes, $\rho = 0$ results will be provided as well. Since notch radius information is often not available [21], $\rho \sim 1.3$ [mm] has been selected as most likely – average – estimate for the data sets with unknown ρ, following previous investigations [20]. Mean stress effects are hardly observed [21], implying differences in fatigue resistance for AW and SR test data is not expected and the parameter vector $\boldsymbol{\Phi} = \{\log(C_{III}), m_{III}, n_{III}, \sigma_{N,III}\}$ is considered to be sufficient.

The obtained most likely intercept and slope, $\log(C_{III}) \sim 16.46$ and $m_{III} \sim 5.02$, are different from the mode-I values (Fig. 10 and Table 1), proving different strength and mechanism contributions. Note m_{III} is similar for the $\rho = 0$ and $\rho > 0$ case and close to a typical design value of 5 [34,72]. Elastoplasticity coefficient n_{III} for $\rho = 0$ is relatively large – even unrealistic – in comparison to the $\rho > 0$ value since notch elastoplasticity increases for decreasing ρ. An interesting observation is that $n_{III} \sim 3.12$ for $\rho > 0$; close to the mode-I value for $\rho = 0$, although the parameter confidence interval is relatively large (Table 1). The parameter confidence bounds suggest that crack growth behaviour can still range from monotonically increasing to non-monotonic (Fig. 7). Most likely the limited variation in data properties as well as the data size are the main reasons. Similar to the S_e based assessment [20], the life time scatter parameter values for $\rho = 0$ and $\rho > 0$ illustrate why the actual notch radius (at the surface) should be included: $\sigma_{N,III}$ reduces from $\sim$0.25 to $\sim$0.21, supporting the hypothesis that the mode-III fatigue damage process might even be more a near-surface phenomenon than for mode-I. Considering the type of loading and geometry reveals a volume (i.e. weld seam length) effect and could partially explain why $\sigma_{N,III}$ turns out to be relatively small in comparison to $\sigma_{N,I}$ [21]. For the mode-I data on the one hand, most specimens are subjected to a bending moment M_b and have a tubular, circular hollow cross-section (Fig. 9). The governing hot spot and most likely fatigue failure position is observed at one location along the weld seam, principally independent of the fabrication aspects induced weakest link; a matter of production tolerances and welding induced defects. On the other hand, for the mode-III data a torsion moment M_t is typically applied and for tubular, circular hollow cross-sections all locations along the weld seam are identified as hot spot. Fatigue failure develops at the position of the fabrication defined weakest link, like the location of the welding induced extreme defect. The mode-III fatigue strength scatter band index $T_{\sigma S_T} = 1 : 1.28$ is smaller than a typical value of $1 : 1.50$ [15].

Like for the uniaxial mode-I assessment, the linear damage accumulation up to $D = 1$ shows VA data fitting the CA data scatter band. A comparison of mode-I and -III data and mean (i.e. 50 [%] reliability) $S_{T,eff} - N$ curves clearly shows differences in both strength and mechanism (Fig. 10), i.e. in $\{\log(C), \gamma\}$ and $\{m, n\}$, implying a lifetime dependent shear strength coefficient $\beta(N)$ rather than a constant one is required for multiaxial fatigue assessment (Section 3.1).

3.3.2. Multiaxial fatigue resistance

Involving the multiaxial fatigue data (Fig. 9), the normal stress equivalent von Mises type of failure criterion is adopted (Eq. 13): $S_T = \sqrt{[S_{T,I}(\gamma_I, n_I)^2 + S_{T,III}(\gamma_{III}, n_{III})^2]}$. Note that for the SS welded butt joints the $S_{T,III}$ related C_{tw} estimate is obtained using the formulation as principally established for DS welded T-joints, assuming $t_c = 0$ [20]. For CA mixed mode-{I, III} data involving asynchronous behaviour and/or different frequencies, as well as for VA multiaxial data, cycle counting in the von Mises plane is initially adopted without any material characteristic non-proportionality effects: $c_m = C_{np} = 0$ (Eq. 14). In order to illustrate the importance of strength and mechanism contributions, reflected in the $\beta(N)$ related $\{\log(C), m\}$ and the mode and material dependent $S_{T,eff}$ parameters $\{\gamma, n\}$, regression analysis results for $\beta = \sqrt{3}$ as well as for $n_I = n_{III}$ are provided for reference purposes (Fig. 11a and Fig. 11b). The parameter vectors have been $\boldsymbol{\Phi} = \{\log(C), S_r, \gamma_{I,AW}, \gamma_{I,SR}, m, n_{I,AW}, n_{I,SR}, n_{III}, \sigma_N\}$ and $\boldsymbol{\Phi} = \{\log(C), S_r, \gamma, m, n, \sigma_N\}$ respectively.

The different strength and mechanism for the uniaxial mode-I and mode-III as well as the multiaxial mode-{I, III} P and NP data can clearly be observed in the separate data scatter bands for $\beta = \sqrt{3}$, reflected in the imaginary intercept and slope for each data group (Fig. 11a). The lifetime scatter parameter $\sigma_N \sim 0.42$ and corresponding strength index $T_{\sigma S_T} = 1 : 2.72$ illustrate in comparison to the uniaxial values: $\sigma_{N,I} \sim 0.30$, $\sigma_{N,III} \sim 0.21$, $T_{\sigma S_T,I} = 1 : 1.75$ and $T_{\sigma S_T,III} = 1 : 1.28$ (Section 3.3.1) a much worse fit. Eliminating in addition the $S_{T,eff}$ related mode and material sensitive strength and mechanism contributions changes the imaginary intercept and slope for each data group (Fig. 11b), although the overall performance basically did not improve: $\sigma_N \sim 0.42$ and $T_{\sigma S_T} = 1 : 2.52$.

However, the scatter of the individual data groups did change. For the uniaxial mode-I and multiaxial mode-{I, III} P data in particular a significant increase and decrease are respectively observed, suggesting the equivalent shear strength and total stress based strength and mechanism contributions are important. The different consequences for uniaxial and multiaxial response conditions even indicate that mode-coupling; an interaction effect, might be involved indeed (Section 1). Overall, the uniaxial mode-I and mode-III as well as the multiaxial mode-{I, III} P data shows a reasonable fit, but the multiaxial mode-{I, III} NP data remains out of range up to a large extent (Fig. 11a and 11b), illustrating at the same time the consequences of data imbalance (Section 3.2). Without affecting the global performance lifetime and strength parameters σ_N and $T_{\sigma S_T}$, the relative position of data groups can change significantly and may cause wrong conclusions regarding the importance of strength and mechanism contributions as observed before [26,39,73].

Adopting the mode specific and material characteristic strength and mechanism contributions; $\{\log(C), m\}$ in terms of $\beta(N)$ – for an iteratively obtained N value (Section 3.1) – and $\{\gamma, n\}$, improves the model performance just up to some extend (Fig. 11c). The lifetime scatter and strength scatter band index reduced a bit: $\sigma_N \sim 0.39$ and $T_{\sigma S_T} = 1 : 2.09$, but are still relatively large in comparison to the uniaxial mode-I data values (Section 3.3.1). At the same time, the multiaxial P and NP data groups still show room for improvement. One reason seems that $\beta(N)$ is not very effective in aligning the scatter bands of the different data groups. For the mid-cycle fatigue range $\beta(N)$ is varying from $\sim$1.2 to $\sim$1.4 and the mean value is $\sim$1.8; quite close to $\beta = \sqrt{3}$ like used for the reference results (Fig. 11a). A similar observation has been made before [39], but seems no argument for a general conclusion since $\beta(N)$ is varying from $\sim$0.5 to $\sim$1.1 for S_e as fatigue strength parameter [21] and performance parameters similar to the mode-I data values are already obtained, whereas for $S_{T,eff}$ a next step is required.

Observing one more time the change in data scatter bands for the reference results from different to similar elastoplasticity coefficients (Fig. 11a and 11b), dedicated ones $\{n_{I,AW,M}, n_{I,SR,M}, n_{III,M}\}$

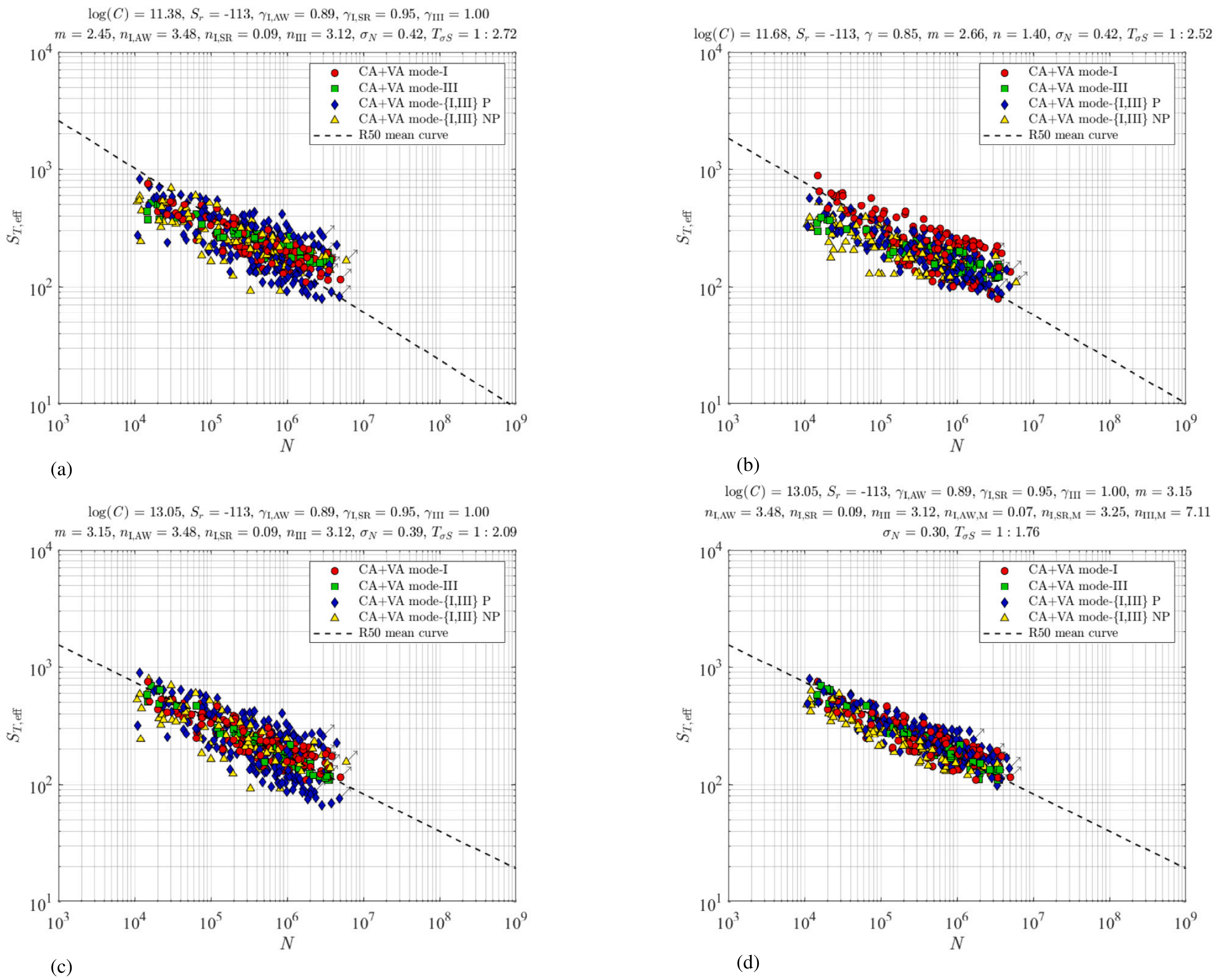

Fig. 11. Total stress based fatigue resistance for uniaxial and multiaxial data adopting: $\beta = \sqrt{3}$ and $\{n_{\mathrm{I}}, \gamma_{\mathrm{I}}\} \neq \{n_{\mathrm{III}}, \gamma_{\mathrm{III}}\}$ (a); $\beta = \sqrt{3}$ and $\{n_{\mathrm{I}}, \gamma_{\mathrm{I}}\} = \{n_{\mathrm{III}}, \gamma_{\mathrm{III}}\}$ (b); $\beta = f(N)$ and $n_{\mathrm{I}} \neq n_{\mathrm{III}}$ for 3 n approach (c) and 6 n approach (d). Note: $c_m = C_{np,i} = 0$.

will be introduced for the mode-{I, III} multiaxial response conditions, reflecting a short crack growth induced mechanism interaction effect. For regression analysis, the parameter vector becomes: $\boldsymbol{\Phi} = \{\gamma_{I,AW}, \gamma_{I,SR}, \gamma_{III}, n_{I,AW}, n_{I,SR}, n_{III}, n_{I,AW,M}, n_{I,SR,M}, n_{III,M}, \sigma_N\}$. Although – in addition to the previously investigated uniaxial mode-I two-stage crack growth characteristics (Section 3.1) – uniaxial mode-III and mixed mode-{I, III} crack growth testing (e.g. using CT specimens) is required to obtain the short crack growth related elastoplasticity coefficients n in order to prove interaction effects, still, most likely n estimates for welded joint fatigue test data are required for verification purposes. Applying one-to-one crack growth based n estimates for welded joint fatigue life time estimates would imply similarity, and proof should be provided. A reversed engineering approach is adopted and most likely n estimates for multiaxial fatigue test data are obtained first in order to reveal the consequences of ignoring interaction effects. Mode-I and mixed mode-{I, III} crack growth tests will be the next step. In case long crack growth mode-{I, III} interaction effects should be incorporated as well, the SIF has to be reformulated including coupling terms (Section 3.1).

Table 2
Total stress and Effective notch stress based $\{n, \rho^*\}$ parameter estimates for multiaxial response conditions, including 75[%] parameter confidence bounds.

	parameter	estimate	75[%] confidence
S_T	$n_{I,AW,M}$	0.07	[0.03, 0.19]
	$n_{I,SR,M}$	3.25	[3.01, 3.59]
	$n_{III,M}$	7.11	[5.07, 9.27]
S_e	$\rho^*_{I,AW,M}$	1.02	[0.17, 2.29]
	$\rho^*_{I,SR,M}$	3.95	[2.77, 5.10]
	$\rho^*_{III,M}$	0.09	[0.01, 1.27]

The most likely multiaxial n estimates are quite different from the uniaxial counterparts and an interpretation of the values seems not straightforward, keeping in mind that the different data groups are not in balance (Section 3.2) and $\{n_{I,AW,M}, n_{I,SR,M}, n_{III,M}\}$ may serve at the same time the purpose of model deficiency correction factor. For mode-I the crack growth behaviour would change from non-monotonic to monotonically increasing and the other way around for respectively the AW and SR data; $\{n_{I,AW} = 3.48, n_{I,AW,M} = 0.07\}$ and $\{n_{I,SR} = 0.09, n_{I,SR,M} = 3.25\}$. Multiaxial response conditions would increase the level of elastoplasticity; for mode-III $n_{III,M} > n_{III}$. The parameters confidence does not look unrealistic (Table 2) and even similar to the uniaxial ones (Table 1). A major achievement is that the life time scatter and strength scatter band index significantly reduced to $\sigma_N \sim 0.30$ and $T_{\sigma S_T} = 1 : 1.76$, supporting the hypothesis of involved interaction effects.

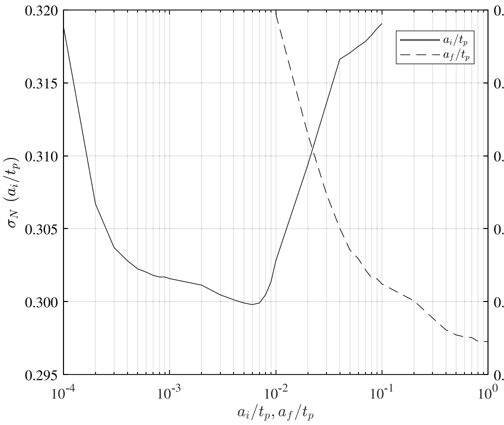

Fig. 12. Most likely σ_N for a range of $a_i/t_p|_{a_f/t_p=1}$ and $a_f/t_p|_{a_i/t_p=0.006}$.

So far, the most likely initial and final crack size values as obtained for the mode-I fatigue resistance of AW joints in planar steel structures are adopted: respectively $(a_i/t_p) \sim 6 \cdot 10^{-3}$ as characteristic defect size and $(a_f/t_p) = 1$ reflecting a through-thickness crack [11]. However, the majority of the considered fatigue resistance data is about welded joints in tubular steel structures (Section 3.2) and welding procedures can be different, explaining why the most likely (a_i/t_p) will be verified with respect to σ_N. Since ρ^* and a_f for respectively $S_{e,eff}$ and $S_{T,eff}$ serve the same purpose (Section 1), (a_f/t_p) will be reconsidered as well. The most likely defect size (a_i/t_p) is still $\sim 6 \cdot 10^{-3}$ (Fig. 12). For the considered fatigue resistance data (Fig. 9) t_p is in between 3.2 and 12.5 [mm], meaning a_i would range from 0.02 to 0.08 [mm], in agreement with typical defect size measurement results [83–85]. Varying (a_f/t_p) for $(a_i/t_p) \sim 6 \cdot 10^{-3}$, $(a_f/t_p) = 1$ still provides the best result, suggesting the stress (intensity) gradient is important for any crack size up to t_p.

Adopting a 0^{th}, 1^{st} or 2^{nd} order moment approach (Section 3.1), differences between the actual response path and the (straight) range have been used to incorporate non-proportionality cycle-by-cycle in terms of C_{np} (Eq. 15), including a material characteristic contribution c_m (Eq. 14). The $c_m - \sigma_N$ sensitivity has been investigated for the C_{np} defined 0^{th}, 1^{st} and 2^{nd} order moment approaches to evaluate the model performance, using the most likely $\{\log(C), S_{r,I}, \gamma_{I,AW}, \gamma_{I,SR}, m, n_{I,AW}, n_{I,AW,M}, n_{I,SR}, n_{I,SR,M}, n_{III}, n_{III,M}\}$ estimates (Fig. 11c and 11d, Tables 1 and 2), $(a_i/t_p) \sim 6 \cdot 10^{-3}$ and $(a_f/t_p) = 1$. Since data is unbalanced, i.e. the multiaxial NP data size is relatively small, the performance for the multiaxial NP data only as well as for all data has been considered. An optimum c_m exists for all approaches and the 1^{st} order one provides the best result (Fig. 13), like for $S_{e,eff}$ [21]. Comparing the total stress and effective notch stress plots, obviously the $S_{T,eff}$ based optimum $c_m \sim 0.40$ is different from the $S_{e,eff}$ related one: $c_m \sim 0.65$, because the fatigue strength parameter is not the same. In contrast to $S_{e,eff}$, the $S_{T,eff}$ optimum for the multiaxial NP data only and all data is not aligned, neither for the 1^{st} order approach nor another one, basically confirming that – like $\{n_{I,AW,M}, n_{I,SR,M}, n_{III,M}\}$ – c_m corrects in addition for any cycle counting and/or non-proportionality related model deficiency. However, $c_m = 1$, suggesting non-proportionality is material invariant, would provide a deficient formulation. Different from $S_{e,eff}$ considering the uniaxial mode and material specific characteristic lengths only (i.e. involving 3 ρ^* parameters), the $S_{T,eff}$ performance for the multiaxial NP data only is even better than for all data, suggesting the distinct elastoplasticity coefficients for multiaxial mode-{I, III} response conditions (i.e. 6 n parameters in total) improves the model performance indeed.

Assessing all data (Fig. 9) using the most likely mode and material specific strength contributions, $\{\log(C), m\}$ and $\{\gamma, n\}$ respectively represented in $\beta(N)$ and $S_{T,eff}$, as well as the 1^{st} order approach to obtain C_{np} cycle by cycle for $c_m \sim 0.40$ in case of non-proportionality, an even better performance is obtained. The lifetime scatter has reduced to $\sigma_N \sim 0.27$ and the strength scatter band to $T_{\sigma S_T} = 1 : 1.66$ (Fig. 14). Principally all data fits the mode-I reference data scatter band, i.e. the interval in between 5 and 95 [%] reliability for 75 [%] confidence. Note that an increased data size: currently ~500 for the assessed data (Fig. 9) and ~2500 for the mode-I reference data, can contribute to another σ_N reduction.

The scatter of the uniaxial mode-I and multiaxial mode-{I, III} P data is about the same and relatively large in comparison to the one of the uniaxial mode-III and multiaxial mode-{I, III} NP data. Although the $S_{T,eff}$ performance is just not equal to that of $S_{e,eff}$ with $\sigma_N \sim 0.26$ and $T_{\sigma S_T} = 1 : 1.65$ [21], the multiaxial mode-{I, III} P data shows a reduced number of outliers and seems a result of the introduced elastoplasticity coefficients $\{n_{I,AW,M}, n_{I,SR,M}, n_{III,M}\}$ for the multiaxial response conditions.

Similarly introducing $\{\rho^*_{I,AW,M}, \rho^*_{I,SR,M}, \rho^*_{III,M}\}$ to incorporate a mechanism interaction effect provides a 6 parameter formulation for $S_{e,eff}$ as well, but hardly improves the performance (Fig. 15a). Whereas $\{n_{I,AW,M}, n_{I,SR,M}, n_{III,M}\}$ and $\{n_{I,AW}, n_{I,SR}, n_{III}\}$ for $S_{T,eff}$ are quite different, the multiaxial $\{\rho^*_{I,AW,M}, \rho^*_{I,SR,M}, \rho^*_{III,M}\}$ estimates are approximately equal to the uniaxial counter parts $\{\rho^*_{I,AW}, \rho^*_{I,SR}, \rho^*_{III}\}$, implying $c_m \sim 0.65$ hardly changes either (Fig. 13). A part of the explanation of ρ^* being less sensitive to mechanism interaction, mode-{I, III} coupling, might be that ρ^* seems to be a more implicit measure; an averaged parameter reflecting a (mixed) mode and material characteristic length in which the majority of the life time has been spent. The (mixed) mode affected elastoplasticity parameter n changes the crack growth behaviour directly (Fig. 7), suggesting n is a more explicit mechanism measure able to provide a better representation of the multiaxial response conditions.

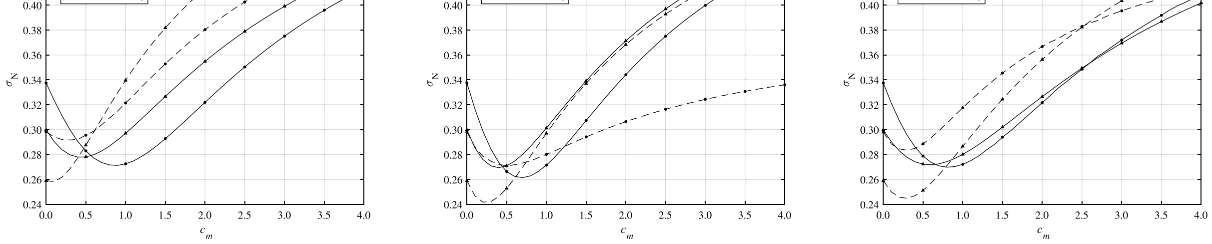

(a) (b) (c)

Fig. 13. Most likely σ_N for a range of c_m. Path dependent non-proportionality: 0^{th} moment (a), 1^{st} moment (b) and 2^{nd} moment (c) for the $S_{T,eff}$ related 6 n approach and the $S_{e,eff}$ related 6 ρ^* approach.

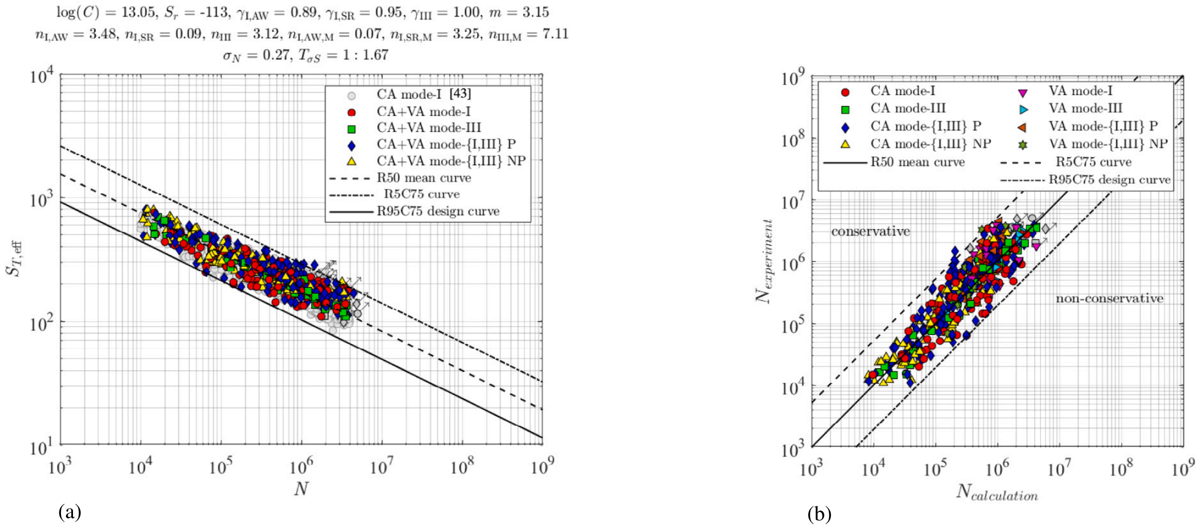

(a) (b)

Fig. 14. Total stress based fatigue resistance (a) and lifetime ratio plot (b) for uniaxial and multiaxial data; $n_{\mathrm{I}} \neq n_{\mathrm{III}}$, $\beta(N)$, 1st order path dependent non-proportionality with $c_m = 0.40$.

Using S_t (Eq. 17), the improved $I_{N,III'}(r_{\tau S})^{1/m_{III}}$ formulation reduces the life time scatter σ_N from 0.36 to 0.32 (Fig. 15 b) and scatter band index $T_{\sigma S_t}$ from 1 : 1.63 to 1 : 1.54. In comparison to $S_{T,eff}$ and $S_{e,eff}$, the S_t performance is a result of the adopted modelling steps with respect to the stress (intensity) distribution (Section 2), the crack growth behaviour and the traction equivalent stress formulation (Section 3.1). The performance of the related S_t based on predominant mode-I crack growth behaviour (Section 3.1), currently $\sigma_N = 0.36$ and $T_{\sigma S_t} = 1 : 2.03$ [26], cannot be improved accordingly, since the mode-III stress intensity formulation is not involved. Note that only a selection of the resistance data (Section 3.2) is included, i.e. the same ∼ 180 SR data points as used before [27,38]. The constant shear strength coefficient $\beta = 3$ explains the average slope value $m \sim 4$ in between $m_I \sim 3$ and $m_{III} \sim 5$, meaning for uniaxial and multiaxial fatigue assessment different resistance curves are used. Since the scatter band index $T_{\sigma S}$ is slope dependent [21], $m \sim 4$ explains at the same time the smaller value for S_t and the larger ones for the mode-I equivalent $S_{T,eff}$ and $S_{e,eff}$.

Overall, the cracked geometry parameter $S_{T,eff}$ and intact geometry parameter $S_{e,eff}$ are able to achieve a similar performance. Looking in particular at the multiaxial P data scatter, an improved multiaxial fatigue strength parameter $S_{T,eff}$ seems still possible, although mode-I formulation advances seems to be a first step since the uniaxial mode-I data scatter is in control (Fig. 10a). However, $S_{T,eff}$ is computationally more expensive because of the $I_N(a/t_p)$ calculation (Section 3.1), whereas $S_{e,eff}$ can be straightforward obtained using an explicit formulation [13,20–22].

The VA data fits the CA data scatter band for $D = 1$ (Fig. 16), supporting the hypothesis that an advanced fatigue failure criterion like $S_{T,eff}$ contributes to an improved (linear) damage accumulation model performance [21].

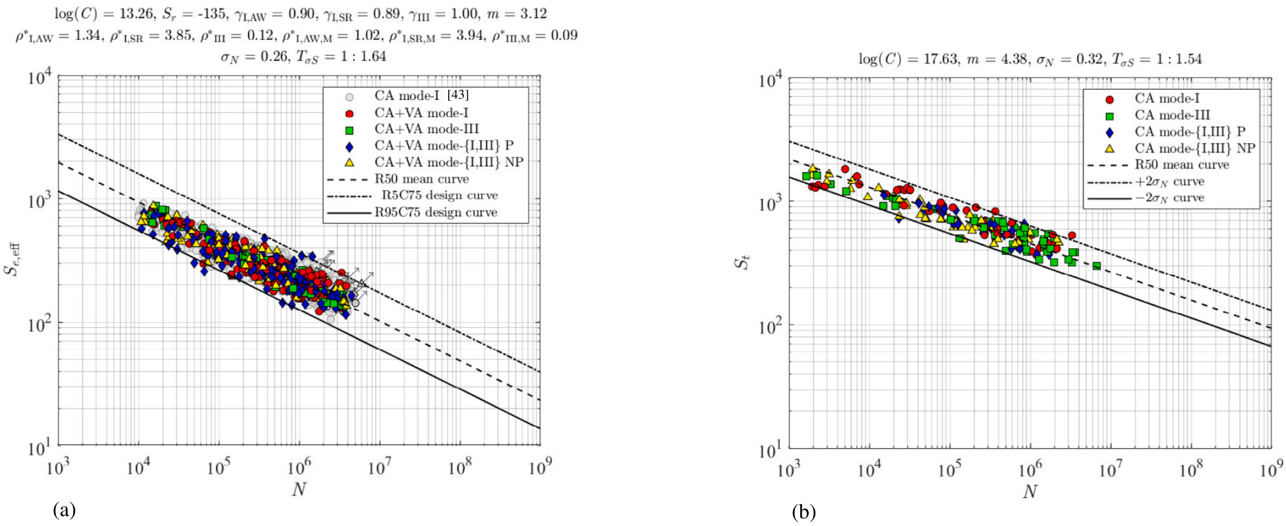

(a) (b)

Fig. 15. Effective notch stress based fatigue resistance for uniaxial and multiaxial data and $\rho^*_{\mathrm{I}} \neq \rho^*_{\mathrm{III}}$, $\beta(N)$, 1st order path dependent non-proportionality with $c_m = 0.65$ (a) and traction equivalent structural stress based fatigue resistance (b).

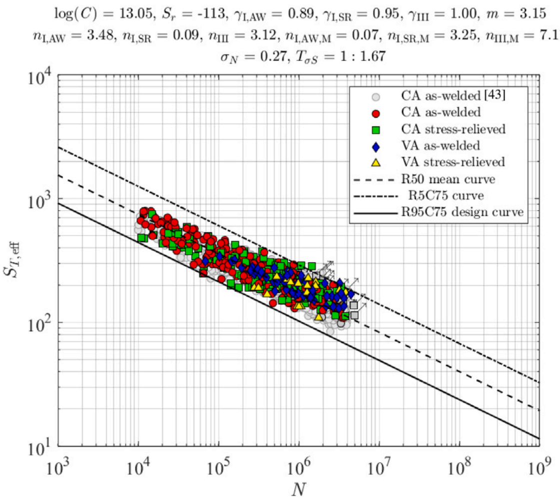

Fig. 16. Total stress based fatigue resistance for uniaxial and multiaxial, constant and variable amplitude, as-welded and stress-relieved data.

4. Conclusions and outlook

Adopting the total stress S_T as SIF based fatigue strength parameter to assess arc-welded joints, dedicated mode-{I, III} far field factor formulations $\{Y_{f,I}, Y_{f,III}\}$ have been established for tubular structures, principally holding for planar ones as an extreme case ($R_t \to \infty$). Good agreement with FE solutions have been obtained.

Uniaxial mode-I and mode-III mid-cycle fatigue resistance investigations revealed distinguished material dependent strength and mechanism contributions in terms of $\{\log(C), \gamma\}$ and $\{m, n\}$, i.e. respectively the resistance curve intercept and mean stress induced response ratio coefficient, resistance curve slope and notch and crack tip elastoplasticity coefficient. For mode-III, the most likely n implicitly suggests (welding residual stress induced) non-monotonic crack growth behaviour, like for mode-I, although the parameter confidence bounds reflects quite some uncertainty and monotonically increasing behaviour could be involved as well. Explicit proof is not available and dedicated mode-III crack growth testing at notches – in particular at different mean stress levels – is recommended.

A von Mises type of failure criterion at the critical fracture plane has been adopted, and a lifetime dependent shear strength coefficient $\beta(N)$ has been introduced to cover the mode specific and material characteristic $\{\log(C), m\}$, whereas S_T explicitly contains $\{\gamma, n\}$. To improve the S_T performance, except 3 uniaxial n parameters, 3 multiaxial ones are introduced, reflecting short crack growth induced mixed mode-{I, III} behaviour. Although the most likely multiaxial n estimates are not straightforward to interpret, the significantly reduced data scatter suggests that interaction effect should be taken into account. Long crack growth mode-{I, III} interaction effects could be incorporated as well and requires a SIF reformulation containing coupling terms. However, the short crack growth contribution seems more important, as reflected in the current S_T performance, because the fatigue life time is predominantly spent in the notch affected region. Mixed mode-{I, III} crack growth testing is required to investigate the two-stage crack growth behaviour and corresponding n values, as well as to address crack growth and fatigue resistance similarity. Embedded in the critical distance theory, the elastoplasticity coefficients are principally response level dependent. Although for mid-cycle fatigue resistance data only the obtained average estimates already provide a constant scatter over the full range, this may change when high-cycle fatigue resistance data will be considered as well. Incorporating a cycle-by-cycle non-proportionality measure with a response path and material contribution, a 1^{st} order response approach shows the best result. The VA data fits the CA data scatter band for $D = 1$.

In comparison to S_e, the S_T performance is similar. The multiaxial P data scatter turns out to be smaller; a consequence of the multiaxial n parameters. Introducing multiaxial ρ^* values for S_e, however, hardly improves the performance, revealing an insensitivity. Whereas n seems to be a more explicit measure directly affecting the crack growth behaviour, ρ^* seems a more implicit measure reflecting the material characteristic length for (mixed) mode and (multiaxial) response conditions. In this respect, S_T can be considered one step closer to the actual physics of the fatigue damage process. In fact, S_T contains with n one more parameter to characterise multiaxiality, since ρ^* for S_e principally serves the same purpose as a_f for S_T. Life time scatter investigations showed that $a_f \to t_p$ rather than $a_f \to \rho^*$ should be used in order to maximise the incorporated stress (intensity) gradient effects and minimise the resistance data scatter. For S_e, a different way to incorporate mixed mode-{I, III} behaviour has to be provided [21].

In order to continue the improvement of the multiaxial fatigue strength parameters S_T or S_e, the mode-I formulation should be re-investigated since the predominantly tubular joint defined uniaxial mode-I data scatter is in control, significantly exceeding the planar joint σ_N value. However, the assessed uniaxial and multiaxial mode-{I, III} data fits the uniaxial mode-I reference data scatter band and a single $S_T - N$ resistance curve can be used for fatigue assessment in engineering applications.

Aiming to incorporate the mode specific characteristics for the traction equivalent stress S_t, the notch to far field transition size should be different for mode-I and mode-III. Fitting the bi-linearised stress distribution approximations suggests $0.1t_p$ to be a good one for mode-III; a smaller notch affected region seems to provide a better fit for mode-I. However, the stress intensity $M_{kn}Y_{f,III}$ requires the opposite in order to obtain a good fit with FE results, suggesting the maximum possible is to incorporate the proposed $Y_{f,III}$ formulation. Improved S_t performance has been obtained accordingly.

CRediT authorship contribution statement

Gabriele Bufalari: Writing – original draft, Visualization, Validation, Software, Methodology, Investigation, Formal analysis, Data curation, Conceptualization. **Henk den Besten:** Writing – review & editing, Supervision, Methodology, Conceptualization. **Jeong Kyun Hong:** Writing – review & editing, Supervision, Methodology, Formal analysis. **Miroslaw Lech Kaminski:** Writing – review & editing, Supervision.

Declaration of competing interest

The authors declare that they have no known competing financial interests or personal relationships that could have appeared to influence the work reported in this paper.

Data availability

The fatigue resistance data used for model validation is available in literature.

Appendix A. Weld notch stress distributions

For mode-I, the self-equilibrium stress part $\sigma_{se}(r/t_p)$ consisting of the V-shaped notch angle characteristic stress and the weld notch load carrying stress components yields:

$$\begin{aligned}\sigma_{se}\left(\frac{r}{t_p}\right) = \left(\frac{r}{t_p}\right)^{\lambda_{\sigma s}-1} \mu_{\sigma s}\lambda_{\sigma s}(\lambda_{\sigma s}+1)\cdot \Big[\cos\{(\lambda_{\sigma s}+1)\beta_a\} + \\ - \chi_{\sigma s}\cos\{(\lambda_{\sigma s}-1)\beta_a\} \Big] + \left(\frac{r}{t_p}\right)^{\lambda_{\sigma a}-1} \mu_{\sigma a}\lambda_{\sigma a}(\lambda_{\sigma a}+1)\cdot \\ [\sin\{(\lambda_{\sigma a}+1)\beta_a\} - \chi_{\sigma a}\sin\{(\lambda_{\sigma a}-1)\beta_a\}] + \\ C_{bw}\left\{ 2\left(\frac{r}{t_p}\right) - 1 \right\}.\end{aligned} \tag{A.1}$$

Plate thickness t_p is either the based plate or the cross plate value: $t_p = t_b$ or $t_p = t_c$, respectively (Fig. 1). Coefficients $\{\mu_s, \mu_a\}$ are obtained using force and moment equilibrium. The involved eigenvalues $\{\lambda_{\sigma s}, \lambda_{\sigma a}\}$, the eigenvalue coefficients $\{\chi_{\sigma s}, \chi_{\sigma a}\}$ as well as the stress angle β_a are notch angle α dependent. The weld notch load carrying stress coefficient C_{bw} is geometry (t_b, t_c, l_w, h_w) and loading (f_n, m_b) dependent and contains the notch stress distribution specific information.

The self-equilibrium stress part $\tau_{se}(r/t_p)$ for mode-III denotes:

$$\tau_{se}\left(\frac{r}{t_p}\right) = \left(\frac{r}{t_p}\right)^{\lambda_\tau - 1} \mu_{\tau F}\cos(\lambda_\tau \beta_a) - (C_{tw} + \mu_{\tau M})\left\{2\left(\frac{r}{t_p}\right) - 1\right\}. \tag{A.2}$$

Coefficients $\{\mu_{\tau F}, \mu_{\tau M}\}$ are force and moment equilibrium defined. Eigenvalue λ_τ is notch angle α dependent. The weld notch load carrying stress coefficient C_{tw} contains the geometry and loading dependent information, providing dedicated notch stress distributions.

Appendix B. Mode-I weld notch stress intensity distributions

The self-equilibrium stress part (Eq. A.1) applied as unit crack face traction along the assumed virtual crack path (Fig. 3) using the weight function approach [41] yields for non-symmetry with respect to $(t_p/2)$ and $\rho = 0$ [13,22]:

$$\begin{aligned} Y_n &= \left(\frac{2}{\pi}\right)\int_0^1 \frac{\sigma_{se}\left(\frac{r}{a}\cdot\frac{a}{t_p}\right) + 1}{\sqrt{1 - \left(\frac{r}{a}\right)^2}}\,\mathrm{d}\left(\frac{r}{a}\right) \\ &= \left(\frac{2}{\pi}\right)\left[\left(\frac{a}{t_p}\right)^{\lambda_{\sigma s} - 1}\mu_{\sigma s}\left(\frac{\sqrt{\pi}}{2}\right)\frac{\Gamma\left(\frac{\lambda_{\sigma s}}{2}\right)}{\Gamma\left(\frac{\lambda_{\sigma s}+1}{2}\right)}\lambda_{\sigma s}(\lambda_{\sigma s} + 1)\cdot\right. \\ &\quad [\cos\{(\lambda_{\sigma s} + 1)\beta_a\} - \chi_{\sigma s}\cos\{(\lambda_{\sigma s} - 1)\beta_a\}] + \\ &\quad \left(\frac{a}{t_p}\right)^{\lambda_{\sigma a} - 1}\mu_{\sigma a}\left(\frac{\sqrt{\pi}}{2}\right)\frac{\Gamma\left(\frac{\lambda_{\sigma a}}{2}\right)}{\Gamma\left(\frac{\lambda_{\sigma a}+1}{2}\right)}\lambda_{\sigma a}(\lambda_{\sigma a} + 1)\cdot \\ &\quad [\sin\{(\lambda_{\sigma a} + 1)\beta_a\} - \chi_{\sigma a}\sin\{(\lambda_{\sigma a} - 1)\beta_a\}] + \\ &\quad \left. C_{bw}\left\{2\left(\frac{a}{t_p}\right) - \frac{\pi}{2}\right\}\right]. \end{aligned} \tag{B.1}$$

The through-thickness crack coordinate (a/t_p) naturally replaced the corresponding through-thickness stress coordinate (r/t_p). The primitives introduce $\Gamma(\cdot)$; the complete gamma function. Formulations for symmetry with respect to $(t_p/2)$ and $\rho > 0$ have been established as well [13,22].

Membrane and bending component formulations defining the linear far field factor for tubular structures, Y_{fm} and Y_{fb} respectively, have been established. Redefining the structural normal stress ratio: $r_{\sigma s} = t_b/(2R_t)$ and fitting FE results provides:

$$Y_{fm} = \eta^{-1}\cdot\left\{A_1\left(\frac{a}{t_b}\right)^4 + A_2\left(\frac{a}{t_b}\right)^3 + A_3\left(\frac{a}{t_b}\right)^2 + A_4\left(\frac{a}{t_b}\right) + A_5\right\} \tag{B.2}$$

with

$A_1 = -0.4102\eta^5 + 5.9416\eta^4 - 31.2763\eta^3 + 74.7289\eta^2 - 76.6080\eta + 32.5525$
$A_2 = 0.3159\eta^5 - 4.7704\eta^4 + 26.4878\eta^3 - 66.1652\eta^2 + 65.8295\eta - 26.0822$
$A_3 = -0.0914\eta^5 + 1.4008\eta^4 - 8.1841\eta^3 + 23.0032\eta^2 - 24.1433\eta + 10.8140$
$A_4 = 0.0072\eta^5 - 0.1105\eta^4 + 0.6432\eta^3 - 1.7606\eta^2 + 2.1383\eta - 0.8209$
$A_5 = 1.0122\eta + 0.0157$

and

$$Y_{fb} = \eta^{-1}\cdot\left\{B_1\left(\frac{a}{t_b}\right)^4 + B_2\left(\frac{a}{t_b}\right)^3 + B_3\left(\frac{a}{t_b}\right)^2 + B_4\left(\frac{a}{t_b}\right) + B_5\right\} \tag{B.3}$$

with

$B_1 = -1.2609\eta^5 + 18.5324\eta^4 - 103.4794\eta^3 + 274.5174\eta^2 - 341.9945\eta + 167.7979$
$B_2 = 0.9786\eta^5 - 14.5248\eta^4 + 82.2228\eta^3 - 220.5391\eta^2 + 272.6368\eta - 132.8441$
$B_3 = -0.2529\eta^5 + 3.8114\eta^4 - 22.2233\eta^3 + 63.1152\eta^2 - 81.0820\eta + 43.6888$
$B_4 = 0.0255\eta^5 - 0.3747\eta^4 + 2.1096\eta^3 - 5.6774\eta^2 + 7.2997\eta - 3.8365$
$B_5 = 1.0123\eta + 0.0164.$

Since the relative membrane and bending contributions are not just loading dependent, a geometry parameter has been introduced: $\eta = -\log\left(\frac{t_b}{2R_t}\right)$. The formulations are applicable for $\{1/2 \leq (t_b/2R_t) \leq 1/200\}$ and $\{0 \leq (a/t_b) \leq 1\}$.

Appendix C. Mode-III weld notch stress intensity distributions

Applying $\tau_{se}(r/t_p)$, the self-equilibrium stress part (Eq. A.2), as unit crack face traction along the assumed virtual crack path using the weight function approach [41] provides for non-symmetry with respect to $(t_p/2)$ and $\rho = 0$:

$$\begin{aligned} Y_n &= \left(\frac{2}{\pi}\right)\int_0^1 \frac{\tau_{se}\left(\frac{r}{a}\cdot\frac{a}{t_p}\right)}{\sqrt{1 - \left(\frac{r}{a}\right)^2}}\,\mathrm{d}\left(\frac{r}{a}\right) \\ &= \left(\frac{2}{\pi}\right)\left[\frac{\left(\frac{a}{t_p}\right)^{\lambda_\tau}\mu_{\tau F}\cos(\lambda_\tau\beta_a)\sqrt{\pi}\,\Gamma\left(\frac{\lambda_\tau}{2}\right)}{2\left(\frac{a}{t_p}\right)\Gamma\left(\frac{\lambda_\tau+1}{2}\right)} - \right. \\ &\quad \left. \frac{\left(\frac{C_{tw}}{2} + \mu_{\tau M}\right)\left(\frac{a}{t_p}\right)\left[\pi - 4\left(\frac{a}{t_p}\right)\right]\Gamma\left(\frac{\lambda_\tau+1}{2}\right)}{2\left(\frac{a}{t_p}\right)\Gamma\left(\frac{\lambda_\tau+1}{2}\right)}\right]. \end{aligned} \tag{C.1}$$

Note that only half the C_{tw} value of the stress distribution (Eq. C.1) is involved for the sake of fitting both the stress as well as the stress intensity.

The linear far field factor shear component

$$Y_{fs}\left(\frac{a}{t_b}\right) = \sqrt{\frac{2t_b}{\pi a}\tan\left(\frac{\pi a}{2t_b}\right)} \tag{C.2}$$

is a handbook solution [86] and the torsion component

$$Y_{ft}\left(\frac{a}{t_b}\right) = \left(C_1\left(\frac{a}{t_b}\right)^4 + C_2\left(\frac{a}{t_b}\right)^3 + C_3\left(\frac{a}{t_b}\right)^2 + C_4\left(\frac{a}{t_b}\right) + C_5\right) \tag{C.3}$$

including

$C_1 = 9.6071\eta^4 - 67.0441\eta^3 + 197.6515\eta^2 - 212.0015\eta + 98.4731$
$C_2 = -15.5960\eta^4 + 108.8379\eta^3 - 320.8629\eta^2 + 344.1559\eta - 131.7393$
$C_3 = 8.8200\eta^4 - 63.3751\eta^3 + 196.7602\eta^2 - 244.8683\eta + 111.5116$
$C_4 = -1.6428\eta^4 + 11.0064\eta^3 - 32.5305\eta^2 + 41.1094\eta - 17.5662$
$C_5 = 0.0522\eta^4 - 0.2881\eta^3 + 0.7159\eta^2 - 0.9626\eta + 1.4579$

a FE fitted formulation. Principally $Y_{f,III}(a/t_p, r_{\tau s})$ is applicable for tubular structures with $\{1/2 \leq (t_b/2R_t) \leq 1/200\}$ and $\{0 \leq (a/t_b) \leq 1\}$, but holds asymptotically for planar ones as well.

Although the real weld notch radius ρ is often virtually zero – justifying the $\rho = 0$ assumption, in some cases the influence of $\rho > 0$ (Fig. 3b) cannot be neglected. The coordinate system origin will be transformed $(O' \rightarrow O)$, keeping the polar axis parallel to the original one:

$$r'^2 = r^2 + 2\cos\left(\beta_a - \theta\right) r_0 r + r_0^2 \tag{C.4}$$

with

$$r_0 = \rho\left(1 - \frac{\pi}{2\alpha}\right).$$

The weight function approach (Eq. C.1) should be modified accordingly ($r \rightarrow r'$) and the τ_{se} formulation [20] denotes:

$$\tau_{se}\left(\frac{r}{t_p}\right) = \left[\left(\frac{r'}{t_p}\right)^{\lambda_\tau - 1}\mu_{\tau F}\cos(\lambda_\tau\beta_a)\left\{1 + \left(\frac{r_0}{t_p}\right)^{2\lambda_\tau}\left(\frac{r'}{t_p}\right)^{-2\lambda_\tau}\right\} - (C_{tw} + \mu_{\tau M})\left\{2\left(\frac{r'}{t_p}\right) - 1\right\}\right] \tag{C.5}$$

with

$$\mu_{\tau F} = -\frac{\lambda_\tau\left\{\mu_{\tau M}\left[\left(\frac{r_0}{t_p}\right)^2 - \left(\frac{r_0}{t_p}\right)\right] - \left(\frac{r_0}{t_p}\right)^2 r_{\tau_s} - 1\right\}}{\cos(\lambda_\tau\beta_a)\left[1 - \left(\frac{r_0}{t_p}\right)^{2\lambda_\tau}\right]}$$

and

$$\mu_{\tau M} = \frac{\begin{gathered}6\lambda_\tau(\lambda_\tau + 1)\left(\frac{r_0}{t_p}\right)^{2\lambda_\tau+1} - 3(\lambda_\tau^2 - 1)\left(\frac{r_0}{t_p}\right)^{2\lambda_\tau+2} - \\ 12\lambda_\tau\left(\frac{r_0}{t_p}\right)^{\lambda_\tau+2} - 3(\lambda_\tau + 1)^2\left(\frac{r_0}{t_p}\right)^{2\lambda_\tau} + 12\lambda_\tau\left(\frac{r_0}{t_p}\right)^{\lambda_\tau+1} + \\ 3\left[\left(\frac{r_0}{t_p}\right) - 1\right](\lambda_\tau - 1)\left\{\left[\left(\frac{r_0}{t_p}\right) - 1\right]\lambda_\tau + \left(\frac{r_0}{t_p}\right) + 1\right\}\end{gathered}}{\begin{gathered}6\lambda_\tau(\lambda_\tau + 1)\left(\frac{r_0}{t_p}\right)^{2\lambda_\tau+1} - (9\lambda_\tau^2 + 6\lambda_\tau - 3)\left(\frac{r_0}{t_p}\right)^{2\lambda_\tau+2} - \\ 12\lambda_\tau\left(\frac{r_0}{t_p}\right)^{\lambda_\tau+2} - (\lambda_\tau^2 - 1)\left(\frac{r_0}{t_p}\right)^{2\lambda_\tau} + 12\lambda_\tau\left(\frac{r_0}{t_p}\right)^{\lambda_\tau+3} + \\ \left\{\left[-4\left(\frac{r_0}{t_p}\right)^3 + 9\left(\frac{r_0}{t_p}\right)^2 + 4\left(\frac{r_0}{t_p}\right)^{2\lambda_\tau+3} - 6\left(\frac{r_0}{t_p}\right) + 1\right]\lambda_\tau - \right. \\ \left. 4\left(\frac{r_0}{t_p}\right)^3 + 3\left(\frac{r_0}{t_p}\right)^2 + 4\left(\frac{r_0}{t_p}\right)^{2\lambda_\tau+3} + 1\right\}(\lambda_\tau - 1)\end{gathered}}.$$

Although the full self-equilibrium stress distribution $\tau_{se}(r/t_b)$ should be involved in order to obtain Y_n, integrating the complete expression does not provide satisfactory results and a simplification is required. The original coordinate system origin transformation (Eq. C.4) is reduced to:

$$r'^2 = r^2 + r_0^2 \tag{C.6}$$

and the $\left\{1 + \left(\frac{r_0}{t_p}\right)^{2\lambda_\tau}\left(\frac{r'}{t_p}\right)^{-2\lambda_\tau}\right\}$ term is excluded. At the same time, for an accurate Y_n definition near the notch, only the exponential term $\left(\frac{r'}{t_p}\right)^{\lambda_\tau - 1}$ needs to be evaluated and the bending equilibrium related term $(C_{tw} + \mu_{\tau M})\left\{2\left(\frac{r'}{t_p}\right) - 1\right\}$ can be excluded from integration. Notch factor Y_n becomes:

$$Y_n\left(\frac{a}{t_p}\right) = \left(\frac{2}{\pi}\right)\int_0^1 \frac{\tau_{se}\left(\frac{r'}{a}\cdot\frac{a}{t_p}\right)}{\sqrt{1 - \left(\frac{r'}{a}\right)^2}}\,\mathrm{d}\left(\frac{r'}{a}\right)$$

$$= \left(\frac{2}{\pi}\right)\int_0^1 \frac{\mu_{\tau F}\cos(\lambda_\tau\theta)\left[\left(\frac{r'}{a}\cdot\frac{a}{t_p}\right)^2 + \left(\frac{r_0}{t_p}\right)^2\right]^{\frac{\lambda_\tau - 1}{2}}}{\sqrt{1 - \left(\frac{r'}{a}\right)^2}}\,\mathrm{d}\left(\frac{r'}{a}\right) - (\mu_{\tau M} + C_{tw})\left\{2\left(\frac{a}{t_p}\right) - \frac{\pi}{2}\right\}$$

$$\begin{aligned}= \left(\frac{2}{\pi}\right)\Bigg\{&\mu_{\tau F}\left(\frac{r_0}{t_b}\right)^{\lambda_\tau - 1}\cos(\lambda_\tau\theta)\sqrt{\pi}r_0\cdot \\ &\Bigg[\Gamma(1 - \lambda_\tau)\,\Gamma\left(\frac{\lambda_\tau}{2}\right)a^{\lambda_\tau}r_0^{-\lambda_\tau}\cdot \\ &{}_2F_1\left(\left[\frac{1 - \lambda_\tau}{2}, \frac{1 - \lambda_\tau}{2}\right]; 1 - \frac{\lambda_\tau}{2}; -\frac{r_0^2}{a^2}\right) + \\ &\Gamma\left(-\frac{\lambda_\tau}{2}\right)\Gamma\left(\frac{\lambda_\tau + 1}{2}\right){}_2F_1\left(\left[\frac{1}{2}, \frac{1}{2}\right]; 1 + \frac{\lambda_\tau}{2}; -\frac{r_0^2}{a^2}\right)\Bigg]\Bigg\}\cdot \\ &\left\{2a\Gamma\left(\frac{1 - \lambda_\tau}{2}\right)\Gamma\left(\frac{\lambda_\tau + 1}{2}\right)\right\}^{-1} - \\ &(\mu_{\tau M} + C_{tw})\left\{2\left(\frac{a}{t_p}\right) - \frac{\pi}{2}\right\}\end{aligned} \tag{C.7}$$

with ${}_2F_1(\cdot)$ representing the Hypergeometric function expression. Note that the $\rho = 0$ formulation (Eq. C.1) is still a $\rho > 0$ limit case. The notch stress intensity in terms of $Y_{n,III}Y_{f,III}$ and K_{III} for the same geometry and loading conditions as provided for $\rho = 0$ (Fig. 5) are shown for illustration purposes (Fig. C.17). A good match with the FE results is obtained.

Weld toe notches appear at both sides of a plate/shell if stress distribution symmetry with respect to $(t_p/2)$ is detected, as shown for a DS welded cruciform joint (Fig. 1). Any influence of another crack at a weld toe notch in the plane of symmetry at $(t_p/2)$ is assumed to be a long crack effect, i.e. considering one notch at the time is sufficient. For an out-of-plane shear force induced response ($\tau_s = \tau_{ss}$), the self-equilibrium stress part of $\tau_s(r/t_p)$ for $\rho = 0$ yields [20]:

$$\tau_{se}\left(\frac{r}{t_p}\right) = \left(\frac{r}{t_p}\right)^{\lambda_\tau - 1}\mu_{\tau F}\cos(\lambda_\tau\beta_a) - \mu_{\tau M}\left\{2\left(\frac{r}{t_p}\right) - 1\right\} - C_{tw}\left\{4\left(\frac{r}{t_p}\right) - 1\right\}. \tag{C.8}$$

For $\rho > 0$, the coordinate system origin must be transformed ($O' \rightarrow O$) like for non-symmetry (Eq. C.4) and becomes:

$$\tau_{se}\left(\frac{r}{t_p}\right) = \left(\frac{r'}{t_p}\right)^{\lambda_\tau - 1}\mu_{\tau F}\cos(\lambda_\tau\beta_a)\left\{1 + \left(\frac{r_0}{t_p}\right)^{2\lambda_\tau}\left(\frac{r'}{t_p}\right)^{-2\lambda_\tau}\right\} - \mu_{\tau M}\left\{2\left(\frac{r'}{t_p}\right) - 1\right\} - C_{tw}\left\{4\left(\frac{r'}{t_p}\right) - 1\right\}. \tag{C.9}$$

To calculate the coefficients $\mu_{\tau F}$ and $\mu_{\tau M}$, half the plate thickness is considered. Using force and moment equilibrium only is principally not sufficient and a symmetry condition has been added as a 3^{rd} equation.

However, the system of equations has become over determined, meaning a least squares solution will be obtained. Allowing for some relaxation, i.e. ignoring moment equilibrium, provides quite accurate results – like for mode-I [22]. Force equilibrium in a weak form and symmetry for $\rho = 0$ provides [21]:

$$\mu_{\tau F} = \frac{\lambda_\tau(C_{tw} + 1)}{\cos(\lambda_\tau\beta_a)\,2^{1-\lambda_\tau}\left(1 + \frac{\lambda_\tau}{2}(\lambda_\tau - 1)\right)} \tag{C.10}$$

and

$$\mu_{\tau M} = \frac{2\lambda_\tau(\lambda_\tau - 1)}{\lambda_\tau^2 - \lambda_\tau + 2} \tag{C.11}$$

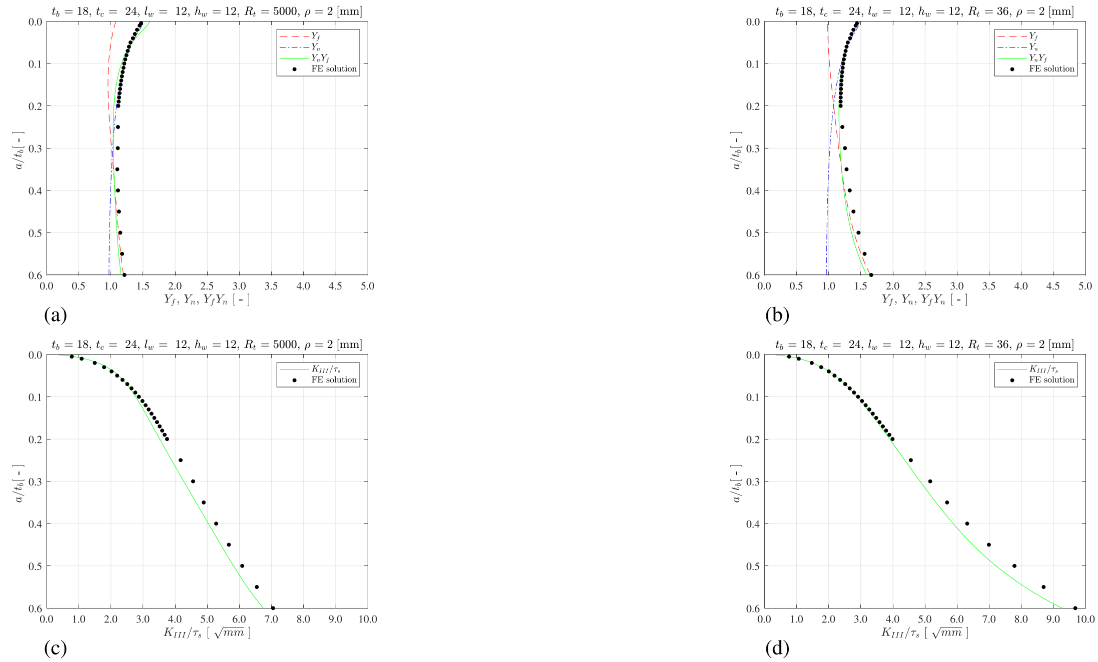

Fig. C.17. Mode-III weld toe notch SIF far field- and notch distribution (a, b) and K_{III} distribution (c, d) for a DS welded T-joint with $\rho > 0$; $r_{\tau_s} = 0$ (a, c), $r_{\tau_s} = 0.25$ (b, d).

and for $\rho > 0$ [21]:

$$\mu_{\tau F} = \frac{\begin{gathered}\lambda_\tau \left\{ \lambda_\tau \left(\frac{r_0}{t_p}\right)^{2\lambda_\tau} \left(\frac{2r_0+1}{2t_p}\right) \left(\frac{4r_0+1}{4t_p^2}\right) \left\{ 2^{\lambda_\tau-1} + C_{tw} 2^{\lambda_\tau} \left(\frac{1}{2t_p}\right) \right\} - \right. \\ 2^{\lambda_\tau+1} C_{tw} \left[\left(\frac{2r_0+1}{2t_p}\right)^2 \left(\frac{r_0}{t_p}\right)^{\lambda_\tau} - \left(\frac{2r_0+1}{2t_p}\right) \left(\frac{r_0}{t_p}\right)^{\lambda_\tau+1} - \left(\frac{2r_0+1}{2t_p}\right)^{2+\lambda_\tau} + \right. \\ \left. \left. \left(\frac{r_0}{t_p}\right) \left(\frac{2r_0+1}{2t_p}\right)^{\lambda_\tau+1} \right] - 2^{\lambda_\tau} \left[\left(\frac{r_0}{t_p}\right)^{\lambda_\tau} \left(\frac{2r_0+1}{2t_p}\right) - \left(\frac{2r_0+1}{2t_p}\right)^{\lambda+1} \right] \right\}\end{gathered}}{\begin{gathered}\cos\left(\lambda_\tau \theta\right) \left(\frac{2r_0+1}{2t_p}\right) \left[\lambda_\tau \left[\left(\frac{4r_0+1}{4t_p^2}\right)\right] \left(\frac{r_0}{t_p}\right)^{2\lambda_\tau} - 2\left(\frac{r_0}{t_p}\right)^{\lambda_\tau} + \right. \\ \left. 2\left(\frac{2r_0+1}{2t_p}\right)^{\lambda_\tau} \right] \left\{ \left(\frac{2r_0+1}{2t_p}\right) \lambda_\tau 2^{\lambda_\tau} \left[\left(\frac{1}{2t_p}\right)\right] \left(\frac{r_0}{t_p}\right)^{2\lambda_\tau} + \right. \\ \left. 2^{\lambda_\tau} \left[\left(\frac{2r_0+1}{2t_p}\right)^{\lambda_\tau} - \left(\frac{r_0}{t_p}\right)^{\lambda_\tau} \right] + \frac{\lambda_\tau(\lambda_\tau-1)}{2t_p^2} \right\}\end{gathered}} \tag{C.12}$$

and

$$\mu_{\tau M} = \frac{\left(\frac{2r_0+1}{2t_p}\right)^2 \lambda_\tau \left\{ 2^{\lambda_\tau} \left(\frac{r_0}{t_p}\right)^{2\lambda_\tau} + 4\left(\lambda_\tau - 1\right) \right\}}{\begin{gathered}\left\{ \lambda_\tau 2^{\lambda_\tau} \left(\frac{r_0}{t_p}\right)^{2\lambda_\tau} \left(\frac{2r_0+1}{4t_p^2}\right) + \right. \\ \left. 2^{\lambda_\tau} \left[\left(\frac{2r_0+1}{2t_p}\right)^{\lambda_\tau} - \left(\frac{r_0}{t_p}\right)^{\lambda_\tau} \right] + \frac{\lambda_\tau(\lambda_\tau-1)}{2t_p^2} \right\}\end{gathered}}. \tag{C.13}$$

Applying the $\tau_{se}(r/t_p)$ formulation (Eq. C.8) as unit crack face traction along the assumed virtual crack path using the weight function approach (Eq. C.1) denotes for $\rho = 0$:

$$\begin{aligned} Y_{n,III,s}\left(\frac{a}{t_p}\right) =& f_{\rho=0}\left(\frac{a}{t_p}\right) \\ =& \frac{\left(\frac{a}{t_p}\right)^{\lambda_\tau} \mu_{\tau F} \cos(\lambda_\tau \beta_a)\sqrt{\pi}\Gamma\left(\frac{\lambda_\tau}{2}\right)}{2\left(\frac{a}{t_p}\right)\Gamma\left(\frac{\lambda_\tau+1}{2}\right)} + \\ & \frac{\left[\left(\frac{a}{t_p}\right)\left(-4\mu_{\tau M} - 8C_{tw}\right) + \pi\left(\mu_{\tau M} + C_{tw}\right)\right]\left(\frac{a}{t_p}\right)\Gamma\left(\frac{\lambda_\tau+1}{2}\right)}{2\left(\frac{a}{t_p}\right)\Gamma\left(\frac{\lambda_\tau+1}{2}\right)}. \end{aligned} \tag{C.14}$$

In case of $\rho > 0$, using the complete $\tau_{se}(r/t_p)$ formulation (Eq. C.9) does not provide satisfactory $Y_{n,III,s}(a/tp)$ results, like for non-symmetry with respect to $(t_p/2)$. Similarly modifying the coordinate system transformation, ignoring the notch affecting term $\{1+(\frac{r_0}{t_p})^{2\lambda_\tau}(\frac{r'}{t_p})^{-2\lambda_\tau}\}$ and excluding the $(\mu_{\tau M}\{2(\frac{r'}{t_p})-1\})$ and $(C_{tw}\{4(\frac{r'}{t_p})-1\})$ terms from transformation for the sake of simplification, the notch factor for an out-of-plane shear force becomes:

$$\begin{aligned} Y_{n,III,s}\left(\frac{a}{t_p}\right) =& f_{\rho>0}\left(\frac{a}{t_p}\right) \\ =& \left(\frac{2}{\pi}\right)\int_0^1 \frac{\mu_{\tau F}\cos(\lambda_\tau\theta)\left[\left(\frac{r'}{a}\cdot\frac{a}{t_p}\right)^2 + \left(\frac{r_0}{t_p}\right)^2\right]^{\frac{\lambda_\tau-1}{2}}}{\sqrt{1-\left(\frac{r'}{a}\right)^2}} \mathrm{d}\left(\frac{r'}{a}\right) - \\ & \mu_{\tau M}\left\{2\left(\frac{a}{t_p}\right) - \frac{\pi}{2}\right\} - C_{tw}\left\{4\left(\frac{a}{t_p}\right) - \frac{\pi}{2}\right\} \\ =& \left(\frac{2}{\pi}\right)\left\{\mu_{\tau F}\left(\frac{r_0}{t_b}\right)^{\lambda_\tau-1}\cos\left(\lambda_\tau\theta\right)\sqrt{\pi}r_0\cdot\right. \end{aligned}$$

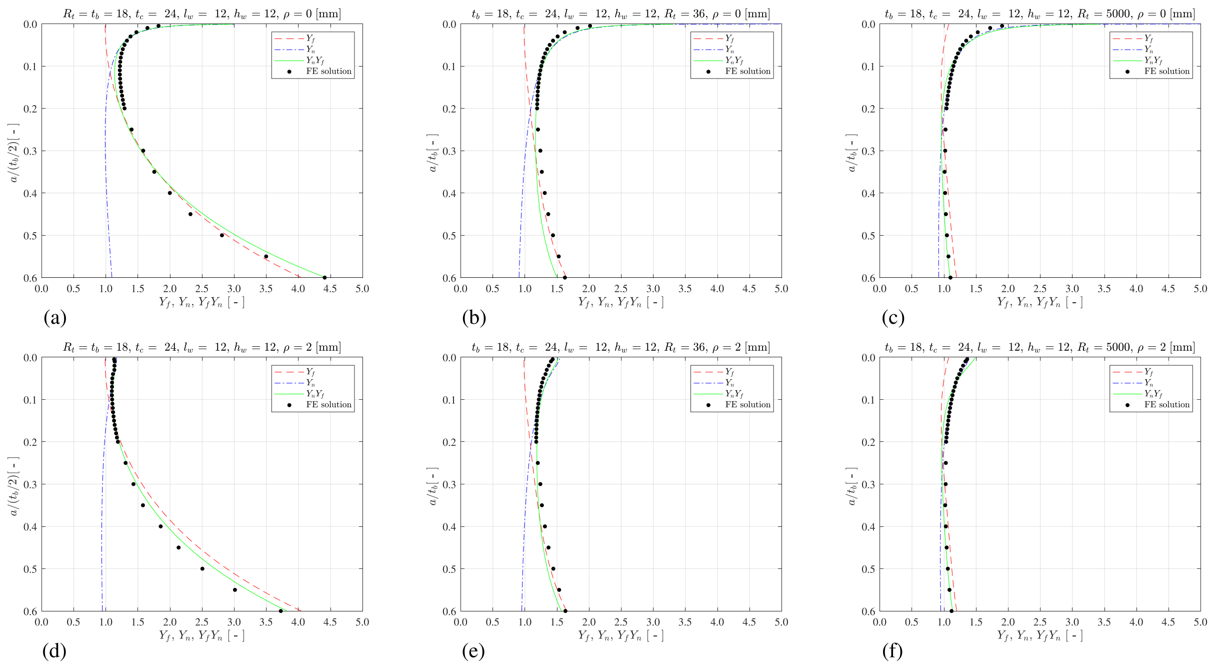

(a) (b) (c)

(d) (e) (f)

Fig. C.18. Weld toe SIF far field- and notch distribution for $\rho = 0$ (a-c) and $\rho > 0$ (d-f) for a DS welded cruciform joint; $r_{\tau_s} = 1$ (a, d), $r_{\tau_s} = 0.25$ (b, e), $r_{\tau_s} = 0$ (c, f).

$$\left[\Gamma\left(1-\lambda_\tau\right)\Gamma\left(\frac{\lambda_\tau}{2}\right) a^{\lambda_\tau} r_0^{-\lambda_\tau} \cdot \right.$$
$$_2F_1\left(\left[\frac{1-\lambda_\tau}{2}, \frac{1-\lambda_\tau}{2}\right]; 1-\frac{\lambda_\tau}{2}; -\frac{r_0^2}{a^2}\right) +$$
$$\left. \Gamma\left(-\frac{\lambda_\tau}{2}\right)\Gamma\left(\frac{\lambda_\tau+1}{2}\right) {}_2F_1\left(\left[\frac{1}{2}, \frac{1}{2}\right]; 1+\frac{\lambda_\tau}{2}; -\frac{r_0^2}{a^2}\right)\right]\Bigg\} \cdot$$
$$\left\{ 2a\Gamma\left(\frac{1-\lambda_\tau}{2}\right)\Gamma\left(\frac{\lambda_\tau+1}{2}\right)\right\}^{-1} -$$
$$\mu_{\tau M}\left\{ 2\left(\frac{a}{t_p}\right) - \frac{\pi}{2}\right\} - C_{tw}\left\{ 4\left(\frac{a}{t_p}\right) - \frac{\pi}{2}\right\}. \qquad \text{(C.15)}$$

For a torsion moment induced response ($\tau_s = \tau_{st}$) the far field torsion stress projection must be included. Like for the $\tau_{ns}(r/t_p)$ formulation [21], $Y_{n,III,s}(a/t_p)$ needs to be shifted first by either $\{1 - f_{\rho=0}(a/t_p = 1/2)\}$ or $\{1 - f_{\rho>0}(a/t_p = 1/2)\}$ in order to meet the condition $\tau_{nt}(r/t_p = 1/2) = 0$. To satisfy anti-symmetry, the τ_{nt} gradient at $(r/t_p = 1/2)$ should be equal to the far field torsion value: -2. Subtracting the shift in terms of a torsion stress gradient $-2\{1 - f_{\rho=0}(r/t_p = 1/2)\}$ or $-2\{1 - f_{\rho>0}(r/t_p = 1/2)\}$ from the unit stress 1, the obtained formulation needs to be scaled using $\{2f_{\rho=0}(r/t_p = 1/2) - 1\}$ or $\{2f_{\rho>0}(r/t_p = 1/2) - 1\}$. For $\rho = 0$, the notch factor yields:

$$Y_{n,III,t}\left(\frac{a}{t_p}\right) = \left(\frac{2}{\pi}\right)\left[2f_{\rho=0}\left(\frac{a}{t_p} = \frac{1}{2}\right) - 1\right]\left\{ f_{\rho=0}\left(\frac{a}{t_p}\right) + \left[1 - f_{\rho=0}\left(\frac{a}{t_p} = \frac{1}{2}\right)\right]\right\} \qquad \text{(C.16)}$$

with

$$f_{\rho=0}\left(\frac{a}{t_p} = \frac{1}{2}\right) = \left(\frac{2}{\pi}\right)\left[\frac{2^{-\lambda_\tau}\mu_{\tau F}\cos(\lambda_\tau\beta_a)\sqrt{\pi}\,\Gamma\left(\frac{\lambda_\tau}{2}\right)}{\Gamma\left(\frac{\lambda_\tau+1}{2}\right)} + \frac{\left[\left(-2\mu_{\tau M} - 4C_{tw}\right) + \pi\left(\mu_{\tau M} + C_{tw}\right)\right]\Gamma\left(\frac{\lambda_\tau+1}{2}\right)}{2\Gamma\left(\frac{\lambda_\tau+1}{2}\right)}\right].$$

In case $\rho > 0$:

$$Y_{n,III,t}\left(\frac{a}{t_p}\right) = \left(\frac{2}{\pi}\right)\left[2f_{\rho>0}\left(\frac{a}{t_p} = \frac{1}{2}\right) - 1\right]\left\{ f_{\rho>0}\left(\frac{a}{t_p}\right) + \left[1 - f_{\rho>0}\left(\frac{a}{t_p} = \frac{1}{2}\right)\right]\right\} \qquad \text{(C.17)}$$

with $f_{\rho>0}(a/t_p = 1/2)$ being numerically obtained (Eq. C.15). Adopting a linear superposition principle for the shear force and torsion moment contributions provides for $\rho = 0$:

$$Y_{n,III}\left(\frac{a}{t_p}\right) = \tau_s\left(\frac{2}{\pi}\right)\left(\left[1 - 2r_{\tau_s}\left\{1 - f_{\rho=0}\left(\frac{a}{t_p} = \frac{1}{2}\right)\right\}\right] f_{\rho=0}\left(\frac{a}{t_p}\right) + \left[2f_{\rho=0}\left(\frac{a}{t_p} = \frac{1}{2}\right) - 1\right]\left[1 - f_{\rho=0}\left(\frac{a}{t_p} = \frac{1}{2}\right)\right]\right). \qquad \text{(C.18)}$$

The same formulation applies for $\rho > 0$, involving $f_{\rho>0}(a/t_p = 1/2)$. Like for non-symmetry with respect to $(t_p/2)$, the $\rho = 0$ formulations are a $\rho > 0$ limit case. For a tubular structure with attachment involving a DS welded cruciform joint and an applied torsion moment M_t (Fig. 1), r_{τ_s} changes for varying R_t. For $R_t \rightarrow t_b$ (reflecting a solid shaft) and $R_t \rightarrow \infty$ (corresponding to a quasi-planar structure), the $(r_{\tau_s} = 1)$ and $(r_{\tau_s} = 0)$ limit cases appear. The performance of the obtained formulations is illustrated (Figs. C.18 and C.19) for both cases as well as for an in between value $(r_{\tau_s} = 0.25)$. In general, the relative error (Fig. C.20) is within 5 [%] for both $Y_{n,III}Y_{f,III}$ and K_{III}, except for $(a/t_p) \rightarrow 0$.

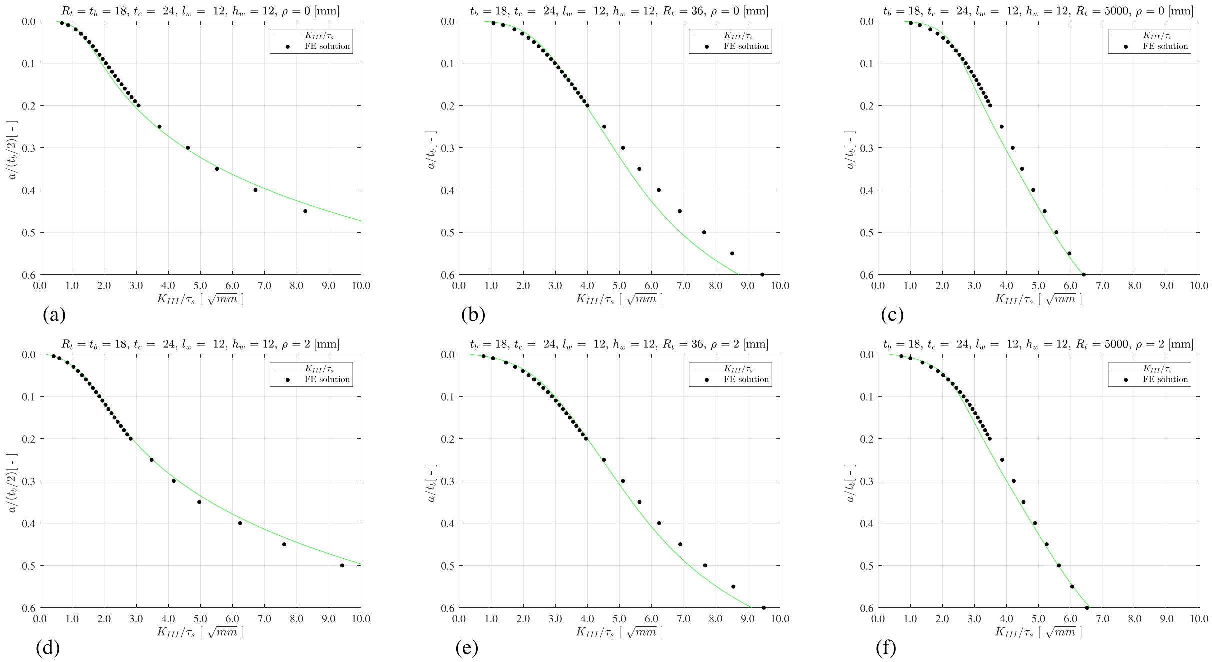

(a) (b) (c)

(d) (e) (f)

Fig. C.19. Weld toe SIF for $\rho = 0$ (a-c) and $\rho > 0$ (d-f) for a DS welded cruciform joint; $r_{\tau_s} = 1$ (a, d), $r_{\tau_s} = 0.25$ (b, e), $r_{\tau_s} = 0$ (c, f).

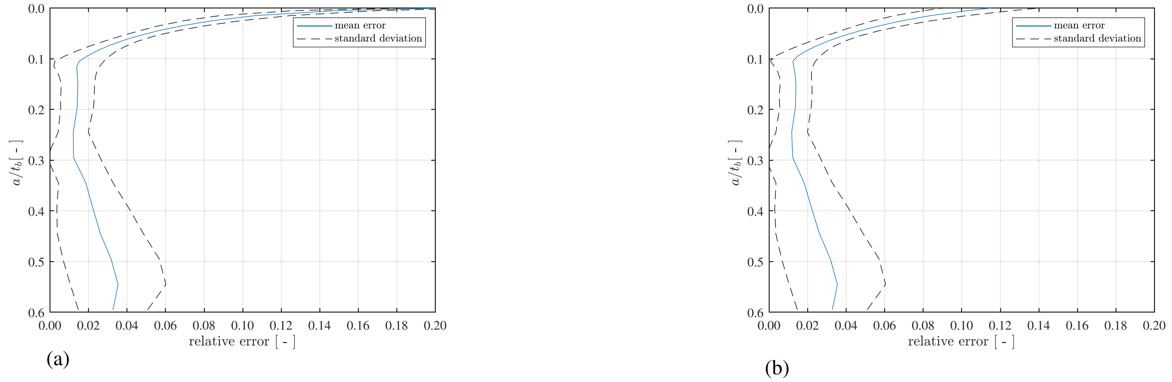

(a) (b)

Fig. C.20. Relative $Y_{n,III}Y_{f,III}$ (a) and K_{III} (b) error for DS welded cruciform joint, comparing the FE solutions and the analytical results for the full parameter application range.

References

[1] Schijve J. Fatigue of structures and materials. Springer Netherlands; 2009.

[2] Bufalari G, Lieshout PV, Kaminski M, Besten JD. Numerical comparative study of multiaxial fatigue methods applied to welded joints in a container vessel. In: 5th symposium on structural durability. Darmstadt; 2017.

[3] Han C, Liu K, Ma Y, Qin P, Zou T. Multiaxial fatigue assessment of jacket-supported offshore wind turbines considering multiple random correlated loads. Renew Energy 2021;169:1252–64. http://dx.doi.org/10.1016/j.renene.2021.01.093.

[4] Reis L, Li B, de Freitas M. A multiaxial fatigue approach to rolling contact fatigue in railways. Int J Fatigue 2014;67:191–202. http://dx.doi.org/10.1016/j.ijfatigue.2014.02.001, Multiaxial Fatigue 2013.

[5] Zhao B, Xie L, Wang L, Hu Z, Zhou S, Bai X. A new multiaxial fatigue life prediction model for aircraft aluminum alloy. Int J Fatigue 2021;143:105993. http://dx.doi.org/10.1016/j.ijfatigue.2020.105993.

[6] Radaj D. Design and analysis of fatigue resistant welded structures. In: Woodhead publishing series in welding and other joining technologies, Cambridge, England: Woodhead Publishing; 1990.

[7] Glen I, Dinovitzer A, Paterson R, Luznik L, Bayley C. Fatigue resistant detail Design Guide for Ship - Ship Structure Committee. U.S. Coast Guard Headquarters.; 1999.

[8] Soares CG, Garbatov Y. Proceedings of 19th international ship and offshore structures congress (ISSC 2015). Mar Struct 2015;74. http://dx.doi.org/10.1016/j.marstruc.2017.09.001.

[9] Lieshout PSV, Besten JHD, Kaminski ML. Multiaxial fatigue assessment of welded joints in marine structures literature overview of progress in academia and engineering practice. Int Shipbuild Prog 2018;65:29–71. http://dx.doi.org/10.3233/ISP-170141.

[10] den Besten J. Fatigue damage criteria classification, modelling developments and trends for welded joints in marine structures. Ships Offshore Struct 2018;13:787–808. http://dx.doi.org/10.1080/17445302.2018.1463609.

[11] Qin Y, den Besten J, Palkar S, Kaminski ML. Mid- and high-cycle fatigue of welded joints in steel marine structures: Effective notch stress and total stress concept evaluations. Int J Fatigue 2021;142:105822. http://dx.doi.org/10.1016/j.ijfatigue.2020.105822.

[12] Lassen T, Recho N. Proposal for a more accurate physically based S-N curve for welded steel joints. Int J Fatigue 2009;31:70–8. http://dx.doi.org/10.1016/j.ijfatigue.2008.03.032.

[13] Qin Y, den Besten H, Palkar S, Kaminski ML. Fatigue design of welded double-sided T-joints and double-sided cruciform joints in steel marine structures: A total stress concept. Fatigue Fract Eng Mater Struct 2019;42:2674–93. http://dx.doi.org/10.1111/ffe.13089.

[14] Neuber H. Kerbspannungslehre. Springer - Verlag; 1937.

[15] Zhang G, Sonsino CM, Sundermeier R. Method of effective stress for fatigue: Part II – Applications to V-notches and seam welds. Int J Fatigue 2012;37:24–40. http://dx.doi.org/10.1016/j.ijfatigue.2011.09.016.

[16] Sonsino CM, Fricke W, Bruyne FD, Hoppe A, Ahmadi A, Zhang G. Notch stress concepts for the fatigue assessment of welded joints - Background and applications. Int J Fatigue 2012;34:2–16. http://dx.doi.org/10.1016/j.ijfatigue.2010.04.011.

[17] Radaj D, Lazzarin P, Berto F. Generalised Neuber concept of fictitious notch rounding. Int J Fatigue 2013;51:105–15. http://dx.doi.org/10.1016/j.ijfatigue.2013.01.005.

[18] Carpinteri A, Boaretto J, Fortese G, Giordani F, Iturrioz I, Ronchei C, et al. Fatigue life estimation of fillet-welded tubular T-joints subjected to multiaxial loading. Int J Fatigue 2017;101:263–70. http://dx.doi.org/10.1016/j.ijfatigue.2016.10.012.

[19] Vantadori S, Iturrioz I, Carpinteri A, Greco F, Ronchei C. A novel procedure for damage evaluation of fillet-welded joints. Int J Fatigue 2020;136. http://dx.doi.org/10.1016/j.ijfatigue.2020.105599.

[20] Bufalari G, den Besten H, Kaminski ML. Mode-III fatigue of welded joints in steel maritime structures: Weld notch shear stress distributions and effective notch stress based resistance. Int J Fatigue 2022;107210. http://dx.doi.org/10.1016/J.IJFATIGUE.2022.107210.

[21] Bufalari G, den Besten H, Kaminski ML. Mode-{I, III} multiaxial fatigue of welded joints in steel maritime structures: Effective notch stress based resistance incorporating strength and mechanism contributions. Int J Fatigue 2024;180:108067. http://dx.doi.org/10.1016/j.ijfatigue.2023.108067.

[22] den Besten J. Fatigue resistance of welded joints in aluminium high-speed craft: A total stress concept [Ph.D. thesis], Delft University of Technology; 2015, p. 1–396.

[23] Dong P. A structural stress definition and numerical implementation for fatigue analysis of welded joints. Int J Fatigue 2001;23:865–76. http://dx.doi.org/10.1016/S0142-1123(01)00055-X.

[24] Dong P. A robust structural stress method for fatigue analysis of ship structures. In: Proceedings of the international conference on offshore mechanics and Arctic engineering - OMAE, vol. 3, American Society of Mechanical Engineers Digital Collection; 2003, p. 199–211. http://dx.doi.org/10.1115/OMAE2003-37313.

[25] Dong P, Hong JK, De Jesus AMP. Analysis of recent fatigue data using the structural stress procedure in ASME div 2 rewrite. J Press Vessel Technol 2006;129(3):355–62. http://dx.doi.org/10.1115/1.2748818.

[26] Mei J, Dong P, Xing S, Vasu A, Ganamet A, Chung J, et al. An overview and comparative assessment of approaches to multi-axial fatigue of welded components in codes and standards. Int J Fatigue 2021;146:106144. http://dx.doi.org/10.1016/j.ijfatigue.2021.106144.

[27] Hong JK, Forte TP. Fatigue evaluation procedures for multiaxial loading in welded structures using battelle structural stress approach. In: Proceedings of the international conference on offshore mechanics and Arctic engineering - OMAE, vol. 5, American Society of Mechanical Engineers Digital Collection; 2014, http://dx.doi.org/10.1115/OMAE2014-23459.

[28] Dong P, Hong JK, Cao Z. Stresses and stress intensities at notches: 'Anomalous crack growth' revisited. Int J Fatigue 2003;25:811–25. http://dx.doi.org/10.1016/S0142-1123(03)00130-0.

[29] Niemi E. Stress determination for fatigue analysis of welded components. Abington in association with the International Institute of Welding; 1995.

[30] Fricke W, Codda M, Feltz O, Garbatov Y, Remes H, Risso G, et al. Round-robin on local stress determination and fatigue assessment of load-carrying fillet-welded joints. In: Advances in marine structures. United States: CRC Press; 2011, p. 295–302.

[31] Rörup J, Maciolowski B, Darie I. FE-based strength analysis of ship structures for a more advanced class approval. In: PRADS 2016 - proceedings of the 13th international symposium on practical design of ships and other floating structures. 2016.

[32] Chattopadhyay A, Glinka G, El-Zein M, Qian J, Formas R. Stress analysis and fatigue of welded structures. Weld World 2011;55(7–8):2–21. http://dx.doi.org/10.1007/BF03321303.

[33] Dong P, Hong JK. The master S-N curve approach to fatigue evaluation of offshore and marine structures. In: 23rd international conference on offshore mechanics and arctic engineering, volume 2. 2004, p. 847–55.

[34] CEN. EN 1993-1-9: Eurocode 3: Design of steel structures - Part 1-9: Fatigue. 2005.

[35] Li Z, Ringsberg JW, Storhaug G. Time-domain fatigue assessment of ship side-shell structures. Int J Fatigue 2013;55:276–90. http://dx.doi.org/10.1016/j.ijfatigue.2013.07.007.

[36] Senjanovic I, Vladimir N, Tomic M, Hadzic N, Malenica S. Global hydroelastic analysis of ultra large container ships by improved beam structural model. Int J Nav Archit Ocean Eng 2014;6(4):1041–63. http://dx.doi.org/10.2478/ijnaoe-2013-0230.

[37] Aygul M. Fatigue analysis of welded structures using the Finite Element method. S.l: Lap Lambert academic publ; 2012.

[38] Hong JK, Forte TP. Fatigue evaluation procedures for bi-axial loaded plate joints using the battelle structural stress method. Procedia Eng 2015;133:410–9. http://dx.doi.org/10.1016/j.proeng.2015.12.611.

[39] Dong P, Wei Z, Hong JK. A path-dependent cycle counting method for variable-amplitude multi-axial loading. Int J Fatigue 2010;32:720–34. http://dx.doi.org/10.1016/j.ijfatigue.2009.10.010.

[40] Mei J, Dong P. An equivalent stress parameter for multi-axial fatigue evaluation of welded components including non-proportional loading effects. Int J Fatigue 2017;101:297–311. http://dx.doi.org/10.1016/j.ijfatigue.2017.01.006.

[41] Bueckner HF. Weight functions and fundamental fields for the penny-shaped and the half-plane crack in three-space. J, Solids Struct 1987;23:57–93.

[42] Dong P, Hong J, Osage D, Prager M. Master S-N curve method for fatigue evaluation of welded components. Weld Res Council Bull 2002;1–44.

[43] Qin Y, den Besten H, Palkar S, Kaminski ML. Weld toe and weld root notch induced fatigue of welded joints in steelmarine structures: Effective notch stress and total stress concept evaluations. Int J Fatigue 2023.

[44] DNV. RP-C203: Fatigue design of offshore steel structures. 2014, p. 126, Recommended Practice DNV-RPC203.

[45] Amsterdam E, Grooteman F. The influence of stress state on the exponent in the power law equation of fatigue crack growth. Int J Fatigue 2016;82:572–8. http://dx.doi.org/10.1016/j.ijfatigue.2015.09.013.

[46] Amsterdam E, Wiegman JW, Nawijn M, Hosson JTMD. The effect of crack length and maximum stress on the fatigue crack growth rates of engineering alloys. Int J Fatigue 2022;161. http://dx.doi.org/10.1016/j.ijfatigue.2022.106919.

[47] Sadananda K, Vasudevan AK. Short crack growth and internal stresses. Int J Fatigue 1997;19:99–108.

[48] Sadananda K, Vasudevan A. Crack tip driving forces and crack growth representation under fatigue. Int J Fatigue 2004;26(1):39–47. http://dx.doi.org/10.1016/S0142-1123(03)00105-1.

[49] Sadananda K, Nani Babu M, Vasudevan A. The unified approach to subcritical crack growth and fracture. Eng Fract Mech 2019;212:238–57. http://dx.doi.org/10.1016/j.engfracmech.2019.03.010.

[50] Kim J-S, Kim C, Jin T-E, Dong P. Mean load effect on fatigue of welded joints using structural stress and fracture mechanics approach. Nucl Eng Technol 2006;38(3):277–84.

[51] Zhou W, Dong P, Lillemäe I, Remes H. Analytical treatment of distortion effects on fatigue behaviors of lightweight shipboard structures. Int J Fatigue 2020;130:105286. http://dx.doi.org/10.1016/j.ijfatigue.2019.105286.

[52] Walker K. The effect of stress ratio during crack propagation and fatigue for 2024-T3 and 7075-T6 aluminum. ASTM International, 1970, http://dx.doi.org/10.1520/stp32032s.

[53] Dong P. Length scale of secondary stresses in fracture and fatigue. Int J Press Vessels Pip 2008;85(3):128–43.

[54] Tschegg EK. Mode III and mode I fatigue crack propagation behaviour under torsional loading. J Mater Sci 1983;18(6):1604–14. http://dx.doi.org/10.1007/bf00542053.

[55] Beretta S, Foletti S, Tarantino MG, Lai J. Comparison between mode I and mode III crack propagation under pure shear and RCF conditions. 2011.

[56] Qi S, Cai LX, Shi KK, Bao C. A prediction model for mode-III fatigue crack growth. Appl Mech Mater 2016;853:41–5. http://dx.doi.org/10.4028/www.scientific.net/amm.853.41.

[57] Duda M, Rozumek D, Lesiuk G, Smolnicki M, Babiarczuk B, Warycha J. Fatigue crack growth under mixed-mode I+II and I+III in heat treated 42crmo4 steel. Int J Fract 2021;234(1–2):235–48. http://dx.doi.org/10.1007/s10704-021-00585-0.

[58] Fonte M, Reis L, Romeiro F, LI B, Freitas M. The effect of steady torsion on fatigue crack growth in shafts. Int J Fatigue 2006;28(5–6):609–17. http://dx.doi.org/10.1016/j.ijfatigue.2005.06.051.

[59] Macha E, Rozumek D. Fatigue crack growth in 18G2A steel under mixed mode I+III loading. European Structural Integrity Society; 2015.

[60] Rozumek D, Marciniak Z, Lesiuk G, Correia JA. Mixed mode I/II/III fatigue crack growth in S355 steel. Procedia Struct Integr 2017;5:896–903. http://dx.doi.org/10.1016/j.prostr.2017.07.125.

[61] Tanaka K. Small fatigue crack propagation in notched components under combined torsional and axial loading. Procedia Eng 2010;2(1):27–46. http://dx.doi.org/10.1016/j.proeng.2010.03.004.

[62] Tanaka K. Crack initiation and propagation in torsional fatigue of circumferentially notched steel bars. Int J Fatigue 2014;58:114–25. http://dx.doi.org/10.1016/j.ijfatigue.2013.01.002.

[63] Vormwald M. Observations and modelling of non-proportional mixed mode cyclic loading. In: MATEC web of conferences, vol. 300, EDP Sciences; 2019, p. 01002. http://dx.doi.org/10.1051/matecconf/201930001002.

[64] Fremy F, Pommier S, Poncelet M, Raka B, Galenne E, Courtin S, et al. Load path effect on fatigue crack propagation in I+II+III mixed mode conditions – part 1: Experimental investigations. Int J Fatigue 2014;62:104–12. http://dx.doi.org/10.1016/j.ijfatigue.2013.06.002.

[65] Predan J, Močilnik V, Gubeljak N. Stress intensity factors for circumferential semi-elliptical surface cracks in a hollow cylinder subjected to pure torsion. Eng Fract Mech 2013;105:152–68. http://dx.doi.org/10.1016/j.engfracmech.2013.03.033.

[66] Rethore J, Gravouil A, Morestin F, Combescure A. Estimation of mixed-mode stress intensity factors using digital image correlation and an interaction integral. Int J Fract 2005;132(1):65–79. http://dx.doi.org/10.1007/s10704-004-8141-4.

[67] Richard H, Eberlein A, Kullmer G. Concepts and experimental results for stable and unstable crack growth under 3D-mixed-mode-loadings. Eng Fract Mech 2017;174:10–20. http://dx.doi.org/10.1016/j.engfracmech.2016.12.005.

[68] Sajith S, Murthy KS, Robi PS. Fatigue life prediction under mixed-mode loading using equivalent stress intensity factor models. In: MATEC web of conferences, vol. 172, EDP Sciences; 2018, http://dx.doi.org/10.1051/matecconf/201817203005.

[69] Schöllmann M, Richard HA, Kullmer G, Fulland M. Int J Fract 2002;117(2):129–41. http://dx.doi.org/10.1023/a:1020980311611.

[70] Liu L. Modeling of mixed-mode fatigue crack propagation [Ph.D. thesis], Vanderbilt University; 2008.

[71] Qian J, Fatemi A. Mixed mode fatigue crack growth: A literature survey. Eng Fract Mech 1996;55(6):969–90. http://dx.doi.org/10.1016/s0013-7944(96)00071-9.

[72] Hobbacher AF. Recommendations for fatigue design of welded joints and components. In: IIW collection, Springer International; 2016.

[73] Wei Z, Dong P, Mei J, Pei X, Ravi SK. A moment of load path-based parameter for modeling multiaxial fatigue damage of welded structures. Int J Fatigue 2023;171:107575. http://dx.doi.org/10.1016/J.IJFATIGUE.2023.107575.

[74] Meggiolaro MA, Castro JTPD. An improved multiaxial rainflow algorithm for non-proportional stress or strain histories - Part I: Enclosing surface methods. Int J Fatigue 2012;42:217–26. http://dx.doi.org/10.1016/j.ijfatigue.2011.10.014.

[75] Mei J, Dong P. A new path-dependent fatigue damage model for non-proportional multi-axial loading. Int J Fatigue 2016;90:210–21. http://dx.doi.org/10.1016/j.ijfatigue.2016.05.010.

[76] Hong JK. Re-evaluation of fatigue evaluation procedures for weld root failure. In: SAE technical paper series. ANNUAL, SAE International; 2019, http://dx.doi.org/10.4271/2019-01-0529.

[77] Yang H, Wang P, Qian H, Dong P. Analysis of fatigue test conditions for reproducing weld toe cracking into U-rib wall in orthotropic bridge decks. Int J Fatigue 2022;162:106976. http://dx.doi.org/10.1016/j.ijfatigue.2022.106976.

[78] Dong P, Hong JK. A robust structural stress parameter for evaluation of multiaxial fatigue of weldments. ASTM Spec Tech Publ 2007;1480 STP:206–22. http://dx.doi.org/10.1520/STP45516S.

[79] Wei Z, Dong P. Multiaxial fatigue life assessment of welded structures. Eng Fract Mech 2010;77(15):3011–21. http://dx.doi.org/10.1016/j.engfracmech.2010.03.045.

[80] Crossland B. Effect of large hydrostatic stress on the torsional fatigue strength of an alloy steel. In: International conference on fatigue of metals. London; 1956, p. 138–49.

[81] Dekking FM, Kraaikamp C, Lopuhaä HP, Meester LE. A modern introduction to probability and statistics: Understanding why and how. Springer - Verlag London; 2005, http://dx.doi.org/10.1198/tech.2007.s502.

[82] Sonsino CM. Multiaxial fatigue of welded joints under in-phase and out-of-phase local strains and stresses. Int J Fatigue 1995;17:55–70. http://dx.doi.org/10.1016/0142-1123(95)93051-3.

[83] Mikulski Z, Lassen T. Fatigue crack initiation and subsequent crack growth in fillet welded steel joints. Int J Fatigue 2019;120:303–18. http://dx.doi.org/10.1016/j.ijfatigue.2018.11.014.

[84] Zerbst U, Madia M, Schork B. Fracture mechanics based determination of the fatigue strength of weldments. Procedia Structural Integrity 2016;1:10–7. http://dx.doi.org/10.1016/j.prostr.2016.02.003.

[85] Zerbst U, Madia M, Vormwald M. Fatigue strength and fracture mechanics. Procedia Struct Integr 2017;5:745–52. http://dx.doi.org/10.1016/j.prostr.2017.07.165.

[86] Tada H, Paris PC, Irwin GR. The stress analysis of cracks handbook. 3rd ed.. ASME Press; 2000, http://dx.doi.org/10.1115/1.801535.